Catalysis Today

Iron porphyrin-derived ordered carbonaceous frameworks

--Manuscript Draft--

Manuscript Number:	CATTOD-D-20-00268R1
Article Type:	SI: ITICAT2019
Keywords:	Ordered carbonaceous frameworks; Iron porphyrin; CO2 reduction; Carbon catalyst; XAFS
Corresponding Author:	Hirotomo Nishihara Tohoku University Sendai, JAPAN
First Author:	Masanori Yamamoto
Order of Authors:	Masanori Yamamoto
	Kazuma Takahashi
	Mao Ohwada
	Yuxin Wu
	Kazuyuki Iwase
	Yuichiro Hayasaka
	Hisashi Konaka
	Henry Cove
	Devis Di Tommaso
	Kazuhide Kamiya
	Jun Maruyama
	Fumito Tani
	Hirotomo Nishihara
Abstract:	Iron-incorporated ordered carbonaceous frameworks (OCFs) have been synthesized by the pyrolysis of iron porphyrin with ethynyl groups as polymerizable/carbonizable moieties at a temperature higher than 600 ºC. The pyrolysis behavior is analyzed by thermogravimetry-differential thermal analysis-mass spectrometry, and the obtained carbon materials are characterized by X-ray diffraction, X-ray absorption fine structure, and high-angle annular dark-field scanning transmission electron microscopy. The introduction of ethynyl groups at the meta positions of the peripheral phenyl groups is essential for efficient cross-linking upon thermal polymerization. The thermally stable polymer thus obtained can be transformed into OCFs with high carbonization yield of 93% at the subsequent carbonization. OCFs possess periodic structural regularity and porphyrin Fe-N 4 coordination structure, and exhibit electrocatalysis for the conversion of CO 2 into CO.

Response to the reviewer #1

Thank you very much for your constructive and precious comment. We have revised the manuscript in accordance with your comment as shown below. In the revised manuscript, the changed part has been highlighted with red colored font. For the Supplementary Information, the changed part is apparent, and I do not highlight them for easier transfer to publication.

Your specific comment:

1. Authors state that the SEM images of the pristine and the annealed mFeP have similar appearance, indicating that the pyrolysis took place with the grain shape well retained even after the carbonization. While, I found the SEM image of the mFeP annealed at 450 ºC (Figure. S3c) is significantly different from the other images.

Response:

Thanks for your comment. We found that *m***FeP** annealed at 450 °C is easily decomposed by an electron beam during the SEM observation. To avoid it, we observed the sample after Pt coating by sputtering. Then, similar structure to those of other samples was successfully observed. Thus, we have replaced the previous SEM image (Fig. S3c) with the newly obtained one as shown below:

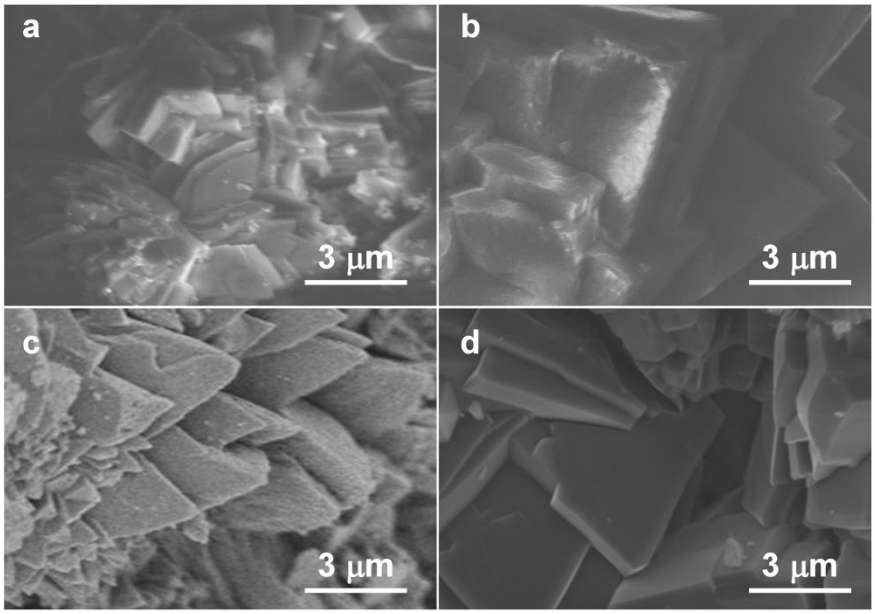

Figure S3. FE-SEM images of *m***FeP** as (a) the pristine crystal and as the treated samples annealed at (b) 270 ºC, (c), 450 ºC, and (c) 600 ºC. Since the sample annealed at 450 °C is easily decomposed

by an electron beam, this sample was observed after Pt coating by sputtering.

2. Authors state that all the pseudo-radial structural functions showed similar shape except for the intensity. However, the peak positions also shift under different temperature. Authors needs to explain this phenomenon.

Response:

The EXAFS patterns are shown below with two dashed lines (light green) for 1st and 2nd peaks of ***m*FeP**.

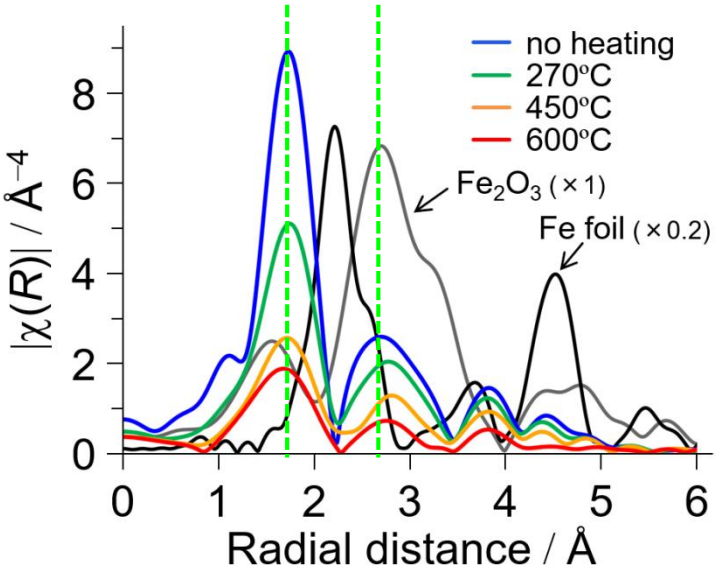

Fig. 5b. EXAFS patterns.

While the peak positions of the 1st peaks are unchanged for annealed samples, the peak positions of the 2nd peaks are gradually shifted, as the reviewer pointed out. This may be due to the structure change of porphyrin framework into carbonaceous framework. Thus, we have revised the text as shown below (changed part is shown in red color):

*For all the samples, the 1st peak of the pseudo-radial structural functions showed similar shape as well as position except for the intensity. Because they differ from Fe metal, oxides, and carbides that has been typically reported to form after the carbonization of porphyrins, we can conclude here that the obtained carbon materials maintains the tetrapyrrole structure where iron center is coordinated by the four pyrrolic nitrogen atoms even after the pyrolysis. This was supported by the well-dispersed C, N, and Fe atoms as confirmed by HAADF-STEM/EDS analysis of m**FeP** annealed*

*at 600 ºC (Fig. S5). From the TG-DTA-MS analysis (Fig. 2a and b), Cl atom was desorbed from Fe center at 300 ºC. Nevertheless, XANES and EXAFS of all m**FeP** derivatives showed similar shape except for the intensity in the EXAFS, indicating the oxidation state of the metal center to be Fe^{III}. The decrease in the intensity of EXAFS upon the heating could be explained by the desorption of heavy Cl atoms with large X-ray scattering from the coordination sphere as well as the increase in the Debye-Waller factor upon the carbonization. On the other hand, the 2nd peak position of m**FeP** is shifted to longer distance with increasing the annealing temperature, and this can be ascribed to the structure change of the porphyrin framework into carbonaceous framework.*

3. For mFeP and FeTPP calcined at different temperature, the total Faradaic efficiency of three products (H2, CO and CH4) are below 100%, is there any other products detected?

Response:

Thanks for an important suggestion. We have confirmed that there is no other product except H_2, CO, and CH_4 during the CO_2 reduction reactions by ^{1}H-NMR and GC-MS. Thus, we have added the following explanation in the main text:

As shown in Fig. S7 and S8, the major products are CO and H_2 for all the samples, and only a trace amount of CH_4 was detected, which coincides with the results of CO_2RR by the reported Fe-based catalysts [5,47].

The data of ^{1}H-NMR and GC-MS have been added in Figure S7 and S8 in the revised version as shown below:

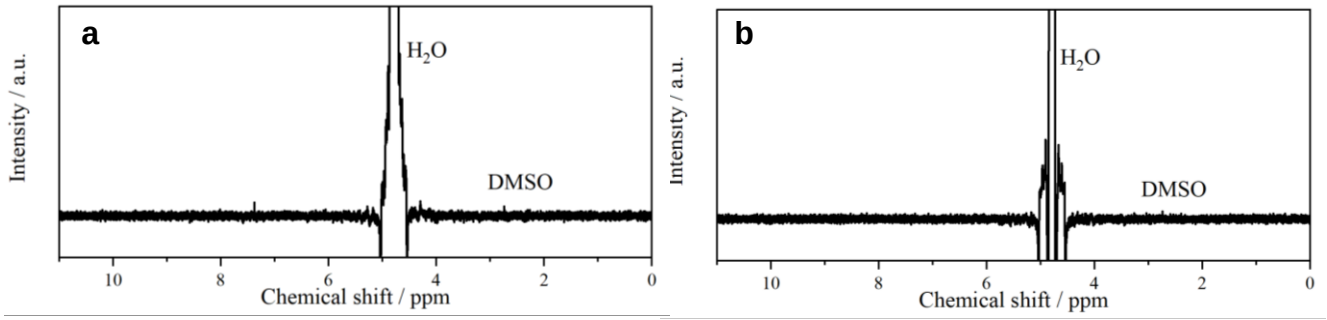

Figure S7. ^{1}H-NMR spectra of electrolytes after electrochemical reduction of CO_2 at -1.0 V vs RHE for 30 min using *m***FeP** annealed at (a) 600 ºC and (b) 700 °C. DMSO was added as an internal standard.

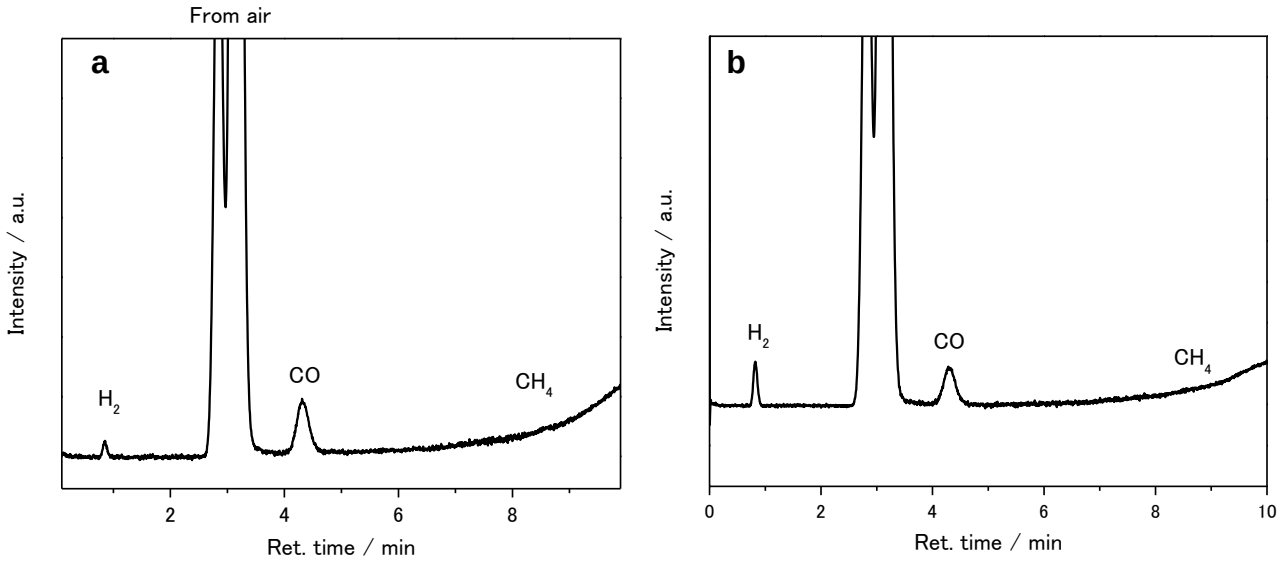

Figure S8. The results of GC-MS during electrochemical reduction of CO_2 (@1.0 V vs RHE, 30 min) using ***m*FeP** annealed at (a) 600 ºC and (b) 700 °C.

The low Faraday efficiency is ascribed to oxygen-reduction reaction caused by a small amount of O_2 which presents as an impurity. Indeed, such a low Faradaic efficiency below 100% is often reported in CO_2 reduction reaction (Angewandte Chemie International Edition, 54, 2146-2150 (2015); Nature communications, 8, 944 (2017); Nature Catalysis, 1, 103-110 (2018); and Advanced Energy Materials, 8, 1801280 (2018)). Thus, we have added the following explanation in the Supporting Information together with the references.

The total of Faraday efficiency is lower than 100% as often reported by other groups [1-4]. This is ascribed to the effect of oxygen-reduction reaction caused by a small amount of O_2 included as an impurity.

[1] J. Choi, P. Wagner, R. Jalili, J. Kim, D.R. MacFarlane, G.G. Wallace, D.L. Officer, Adv. Energy Mater. 8 (2018) 1801280.

[2] P. De Luna, R. Quintero-Bermudez, C.-T. Dinh, M.B. Ross, O.S. Bushuyev, P. Todorović, T. Regier, S.O. Kelley, P. Yang, E.H. Sargent, Nat. Catal. 1 (2018) 103-110.

[3] W. Ju, A. Bagger, G.-P. Hao, A.S. Varela, I. Sinev, V. Bon, B. Roldan Cuenya, S. Kaskel, J.

Rossmeisl, P. Strasser, Nat. Commun. 8 (2017) 944.

[4] S. Rasul, D.H. Anjum, A. Jedidi, Y. Minenkov, L. Cavallo, K. Takanabe, Angew. Chem. Int. Ed. 54 (2015) 2146-2150.

4. There are many detail mistakes in the article, the author should check them carefully. For example, 'In Fig. 3a, mFeP shows an exothermic peak at 305 °C, corresponding to thermal polymerization of ethynyl groups' should be Fig. 2a, and a lot of problems like that.

Response:

Thanks for pointing out the mistake. We have thoroughly check the entire manuscript and made corrections

Response to the reviewer #2

Thank you very much for your constructive and precious comments. We have revised our manuscript in accordance with your opinions as shown below. In the revised manuscript, the changed part has been highlighted with red colored font. For the Supplementary Information, the changed part is apparent, and I do not highlight them for easier transfer to publication.

Your specific comments:

1. The carbonization temperature used is 600ºC. The most probable is that the electrical conductivity will not be high. Is it enough for a possible application as electrocatalyst? The electrochemical characterization is done using a thin film, making this property not so relevant. However, it can be important to improve the electron transfer rate.

Response:

Thanks for your important comment. We have examined the electrocatalysis of the samples prepared at 600 °C and 700 °C in this work. However, we didn't explain the effect of the annealing temperature in the previous version. As you pointed out, annealing at 700 °C can improve the electric conductivity and it is expected to enhance the electrocatalytic performance. However, *m***FeP** annealed at 700 °C actually showed much lower activity for CO_2RRs compared to *m***FeP** annealed at 600 °C. This can be ascribed to the destruction of the porphyrin structure in 700 °C as shown in Fig. 3a. Thus, we have added the following sentences in the revised version:

*The CO_2RRs were performed also on m**FeP** and **FeTPP** annealed at 700 °C. All the results were summarized in Table S2-5. As shown in Fig. S7 and S8, the major products are CO and H_2 for all the samples, and only a trace amount of CH_4 was detected. While Ni-based OCF synthesized at 600 °C can achieve a good CO_2RR catalysis [31], higher annealing temperature of 700 °C provides better electric conductivity [27] which is preferable for superior performance. However, m**FeP** annealed at 700 °C without ordered structure (Fig. 3a) showed much lower activity for CO_2RRs compared to the sample annealed at 600 °C. This also indicates the significance of the porphyrin-structure retention for the CO_2RRs activity.*

Moreover, the calculation results suggest that poor electric conductivity may cause low Faraday efficiency. In the previous version, this point was not well explained. Thus, we have added the following explanation:

*At the same time, two problems have emerged regarding effective CO_2 conversion. One of them is not sufficient electric conductivity of OCF annealed at 600 °C. The calculations demonstrated thermodynamically favored catalysis on well-reduced Fe sites, while less-reduced Fe sites cause hydrogen evolution. The lack of electric conductivity thus causes low FE in electrochemical CO_2 conversion. To improve the electric conductivity, application of higher annealing temperature is effective [27], whereas the fine chemical structure of m**FeP** collapses at 700 °C, resulting in very low FE (Table S3). To overcome this problem, it is necessary to improve the thermal stability of crystalline polymer which is formed as an intermediate of OCF.*

To overcome the problem of low electric conductivity, a new molecular design is necessary. Indeed, we are working on such a new idea now. Thus, we have added the following comment at the end of the main text:

Unlike the conventional carbonaceous catalysts, the OCF synthesis allows a precise molecular design based on the techniques of organic chemistry, and there is plenty of room for improvement [26]. For instance, introduction of a larger number of ethynyl groups to the porphyrin framework may be effective to form highly developed three-dimensional crosslinking and its translation into highly porous OCFs. The developed crosslinking is also expected to achieve an improved thermal stability of the framework, enabling higher annealing temperature to enhance the electric conductivity of OCFs. Such new tactics is under investigation.

2. The authors should add more information about the experimental details of the electrochemical characterization. This would make easier for the readers of this work rather than looking for that information in another manuscript.

Response:

We thought that we have described the details of the electrochemical characterization, enough for others to reproduce our experiment. One of the reasons for the reviewer's suggestion may be the first sentence of the "2.4. Electrochemistry": "The activities of the annealed *m***FeP** and reference samples for electrochemical reduction of CO_2 were evaluated based on the method reported elsewhere [35]." We have actually described the details of experimental techniques in the original manuscript (see page 5 of the revised manuscript), and a reader does not need to refer to the reference [35]. Thus, we have revised

this sentence as shown below:

*The activities of the annealed m**FeP** and reference samples for electrochemical reduction of CO_2 were evaluated based on the method previously established [35].*

Moreover, we have added some more information: how to polish a GC electrode and volumes of liquid and vapor phases in the three-electrode cell as shown below:

Prior to casting the catalyst ink, a GC electrode was sequentially polished with 1.00 and 0.05 μm aluminum suspensions.
The volumes of catholyte and gas phase are 13 and 4.4 ml, respectively, in the three-electrode cell.

3. Cyclic voltammograms (CV) for the different materials tested as electrocatalysts should be included and discussed. This is important information to observe differences among the materials.

Response:

Cyclic voltammograms are basic information of electrochemistry, and we can understand the reviewers comment. Thus, we have performed cyclic voltammetry and added the results in Figure S6 in the revised version as shown below:

6. *Cyclic voltammograms*

(a) ***m*Fe** annealed at 600 ºC

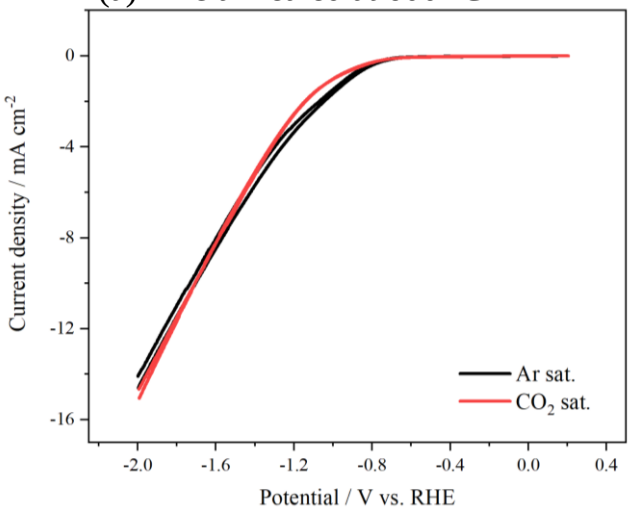

(b) ***m*Fe** annealed at 700 ºC

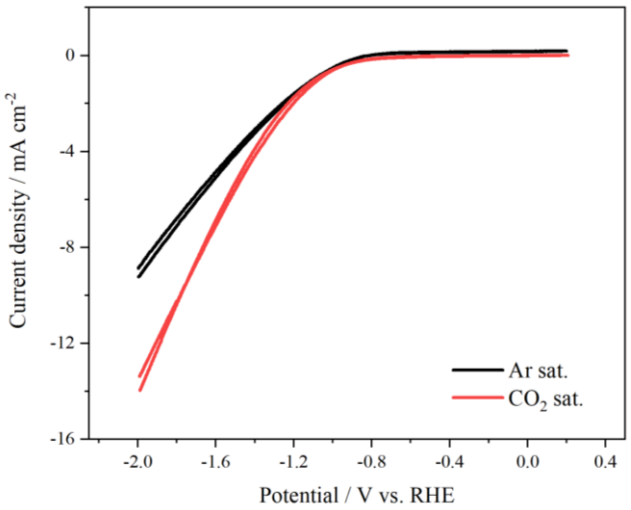

(c) **FeTPP** annealed at 600 ºC

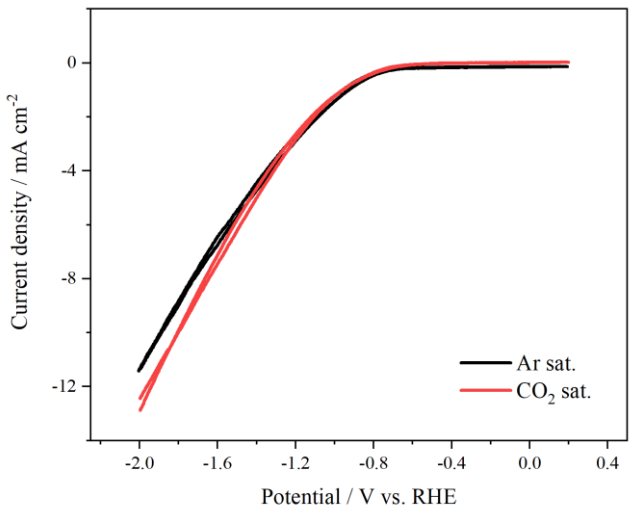

(d) **FeTPP** annealed at 700 ºC

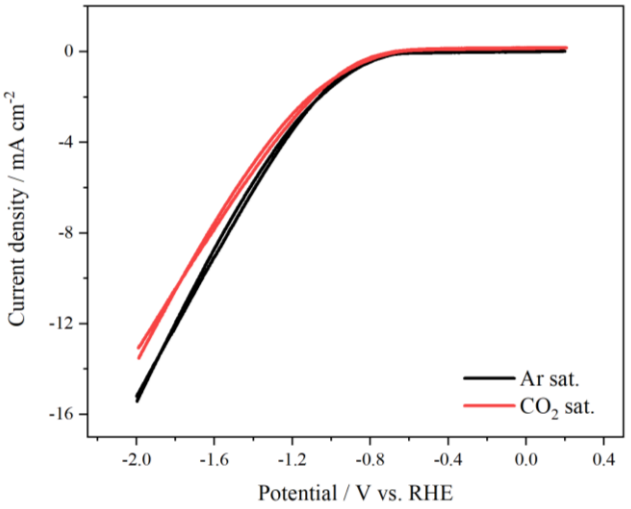

Figure S6. Cyclic voltammograms measured in 0.1 M phosphate buffer saturated with Ar and in 0.1 M $KHCO_3$ saturated with CO_2 (pH 6.8) for (a) ***m*FeP** annealed at 600 °C, (b) ***m*FeP** annealed at 700 °C, (c) **FeTPP** annealed at 600 °C, and (d) **FeTPP** annealed at 700 °C. Scan rate is 10 mV s^{-1}.

Without the presence of CO_2, all the samples showed current increase below –0.8 V due to hydrogen evolution reactions. Only in ***m*FeP** annealed at 600 °C, current decrease was observed around –0.9 to –1.5 V when CO_2 was introduced. A possible reason for the current decrease is the occurrence of CO_2RRs on the same catalytic sites which were used for hydrogen evolution reactions, and additionally, the activity of CO_2RRs is not significantly high. However, much more detail discussion is difficult only using the cyclic voltammograms because of the effect of the hydrogen evolution reactions. Thus, we have added the following text in the revised manuscript:

*The basic electrocatalytic behaviors of m**FeP** annealed at 600 and 700 °C were examined by cyclic voltammetry with and without the presence of CO_2 (Fig. S6). For comparison, **FeTTP** annealed at 600 and 700 °C were also investigated. Without the presence of CO_2, all the samples showed current increase below –0.8 V due to hydrogen evolution reactions. Only in m**FeP** annealed at 600 °C, current decrease was observed around –0.9 to –1.5 V when CO_2 was introduced. A possible reason for the current decrease is the occurrence of CO_2RRs on the same catalytic sites which were used for hydrogen evolution reactions, and additionally, the activity of CO_2RRs is not significantly high. However, detail discussion is difficult only using the cyclic voltammograms.*

4. This reviewer has not found the meaning of FeTPP. It should be included.

Response:

We are sorry for this mistake. **FeTPP** is used as an abbreviation for tetraphenylporphyrin iron(III) chloride. We have spelled out **FeTPP** in the introduction as shown below:

*Finally, the electrochemical reduction of CO_2 has been investigated using the OCFs and reference carbonaceous materials derived from tetraphenylporphyrin iron(III) chloride (**FeTPP**, Fig. 1), and the importance of the initial association between reduced Fe species and CO_2 was corroborated by means of density functional theory calculations.*

5. Section 2.4: The authors write "The activities of the annealed mFeP and reference samples for electrochemical reduction of CO2 were evaluated…" Why pFeP derived samples have not been evaluated?

Response:

The difference between the *m***FeP**-derived sample and the *p***FeP**-derived sample is the presence of porphyrin-derived fine chemical structures in the former. We have actually examined electrocatalysis of four samples, (1) 600 ℃-annealed *m***FeP**, (2) 700 ℃-annealed *m***FeP**, (3) 600 ℃-annealed **FeTPP**, and (4) 700 ℃-annealed **FeTPP**. Only (1) is the OCF with porphyrin-derived fine chemical structures, and other three samples are counterparts without such fine structures. So, comparison between these samples is enough to prove the significance of the unique structure of (1). However, in the previous version, we didn't clearly explain the meaning of "FeTPP" as the reviewer pointed out in the comment #4. Additionally, we have not explained the electrocatalysis of these four samples in detail. In the revised manuscript, we have fixed these problems as we have described in the answers for the reviewer's comment #1 and #4. Of course, the inclusion of the electrocatalysis data of *p***FeP** is better, but it requires a great effort and not small amount of experiments. Especially under the severe restriction caused by the COVID-19, it is very difficult for us to complete these experiments within a reasonable period. As described above, even without the data of *p***FeP**, the significance of the present OCF material has been already proved by using other counterpart materials, and we believe that the necessity of the data of *p***FeP** is not crucial in the present work.

6. Quantum chemical calculations: There are two doubts for this section. The first one is that considering that the reaction requires some overpotential to occur, how do the calculations change if the authors consider the effect of potential? The second doubt is that the authors consider the CO2 molecule but, really, what they have in solution and with a much higher concentration is HCO3- anions. How do the calculations change considering this species? Would the initial state of the catalyst have any influence in the different steps?

Response to the **first comment**:

An established approach to consider the effect of overpotential on the reaction profiles of an electrochemical reaction is the computational hydrogen electrode (CHE) model proposed by Nørskov and co-workers [J. Phys. Chem. B 2004, 108, 17886-17892; J. Electroanal. Chem, 2007, 20, 83–89], which has been used in most simulations of heterogeneous electrocatalysis. However, the CHE model is restricted to steps in which an equal number of protons and electrons are transferred (concerted

proton−electron process).

The three reaction pathways considered in this study (see below) are based on the CO_2 reduction cycle suggested for iron-porphyrin catalysts by Chang et al. (*Chem. Sci.* 2018, 9, 2952−2960) and by Davethu and de Visser (J. Phys. Chem. A 2019, 123, 6527−6535), where the protonation (**2** and **3**) and electron transfer (**4** and **5**) elementary steps do not occur simultaneously (full discussion in Section 10 of **Supplementary Information**). The CHE model cannot, therefore, be applied to compute the potential free energy profiles.

The main objective of the density functional theory (DFT) calculations reported in this study is to understand the most stable oxidation state of the Fe centre upon which the CO_2 adsorption takes place, rather the quantifying the effect of the electrochemical potential.

Thus, the following text has been added on pages 9-10 of revised version of the manuscript:

*One of the key factors underlying the catalytic performance of electrocatalysts for CO_2 reduction is the interaction between the adsorbate and the metal-organic complex [47]. Therefore, in order to understand the effect of the oxidation state of the Fe center on the electrochemical conversion of CO_2 to CO, we have conducted DFT calculations of the mechanism of CO_2 reduction catalysed by iron porphine [FeP] with the CO_2 adsorption taking placing on the following three complexes: the doubly negative $[FeP]^{-2}$, the singly negative $[FeP]^{-}$, and the neutral $[FeP]^{0}$ (see Supporting Information and Table S6). Simulations showed that the Fe porphine-CO_2 complex is thermodynamically unfavoured starting from $[FeP]^{0}$ and $[FeP]^{-}$ (Fig. 7b). Thus, the coordination of CO_2 to $[FeP]^{0}$ and $[FeP]^{-}$ will be rather uphill and less feasible, and this could lead to H_2 evolution to be kinetically dominant. Fig. 7b shows that initial step of CO_2 conversion to *COOH could be further inhibited by the weak COOH binding to the $[FeP]^{0}$. On the contrary, the more favourable association of CO_2 (1 kJ.mol^{-1}) and strong stabilization of *COOH on the $[FeP]^{2-}$ complex (-64 kJ mol^{-1}) suggest that higher Faraday efficiencies could be achieved under electrochemical conditions promoting well-reduced Fe species (Table S7).*

Response to the **second comment**:

The referee is raising an interesting point. To the best of our knowledge, computational studies of CO_2 reduction reactions in aqueous environments have not considered, so far, the possible role of bicarbonate ions in the reaction mechanism. Therefore, we have conducted further calculations to model the adsorption of the HCO_3^- molecule on the $[FeP]^0$, $[FeP]^-$ and $[FeP]^{2-}$ complexes. Calculations have been

conducted at the DFT (UB3LYP-D3/6-311G++(d,p)) level, using the CPCM implicit solvation model to treat the aqueous environment.

Comparison of the results for HCO_3^- and CO_2 in **Table S8** show very similar energetics for the adsorption on the iron porphine complexes $[FeP]^0$, $[FeP]^-$, and $[FeP]^{2-}$. Also, the adsorption step of these two molecules onto the metal centre appears to be marginally endergonic ($\Delta G > 0$) along all reaction pathways. In the initial process of CO_2 binding to the active site of the catalyst, there could be some competition with the bicarbonate molecule.

Table S8. Comparison of the energetics of adsorption of the bicarbonate (HCO_3^-) and carbon dioxide (CO_2) molecules on the iron complexes $[FeP]^0$, $[FeP]^-$ and $[FeP]^{2-}$ as calculated at the DFT (UB3LYP-D3/6-311G++(d,p)) level using the CPCM implicit solvation model (water). Values in kJ mol^{-1}.

	ΔE	ΔE + ZPE	ΔG
Pathway 1			
$[Fe]^0 + HCO_3^- + H_2O \rightarrow [Fe(CO_3H)]^-$	-5.65	-4.73	6.85
$[Fe]^0 + CO_2 \rightarrow [Fe(CO_2)]^0$	-4.17	-3.37	5.73
Pathway 2			
$[Fe]^- + HCO_3^- \rightarrow [Fe(CO_3H)]^{2-}$	-4.63	-0.73	10.42
$[Fe]^- + CO_2 + \rightarrow [Fe(CO_2)]^-$	-3.34	0.23	11.55
Pathway 3			
$[Fe]^{2-} + HCO_3^- \rightarrow [Fe(CO_3H)]^{3-}$	-14.27	-13.95	0.32
$[Fe]^{2-} + CO_2 \rightarrow [Fe(CO_2)]^{2-}$	-12.01	-10.32	1.01

We have added **Table S8** in Supporting Information. The values of the absolute (free) energies (in Hartree) of the $^3[Fe(HCO_3)]^-$, $^2[Fe(HCO_3)]^{2-}$, and $^3[Fe(HCO_3)]^{3-}$ systems have also been included in **Table S6**.

Moreover, the following text has been added on page 9 of revised version of the manuscript:

Because in aqueous solutions, there is a higher concentration of bicarbonate (HCO_3^-) than CO_2, we have also computed the interaction of HCO_3^- with the iron porphine complexes. The (free) energies of adsorption of HCO_3^- on $[FeP]^0$, $[FeP]^-$ and $[FeP]^{2-}$ are marginally endergonic ($\Delta G > 0$) and similar in value to the values computed for the CO_2 molecule (Table S8). In the initial process of CO_2 binding to the active site of the catalyst, there could be some competition with the bicarbonate molecule.

7. The characterization of the porosity must be included. In the case of m-FeP, probably the porosity is much higher or more accessible to CO2. Thus higher amount of Fe sites can be available what can explain the higher catalytic activity. Maybe, the porosity for p-FeP is much lower but the activity per accessible site can be similar. All this should be discussed including porosity data and proper electrochemical characterization data (for example CV can be very helpful).

Response:

Thanks for your important comment. We have included the porosity data of ***m*FeP** and ***p*FeP** after annealing as Table S1 in the revised manuscript.

Table S1. Porosity of ***m*FeP** and ***p*FeP** after annealing.

Sample (annealing temperature)	BET surface area ($m^2\ g^{-1}$)	V_{N2} ($cm^3\ g^{-1}$)	V_{CO2} ($cm^3\ g^{-1}$)
***m*FeP** (450 °C)	0	0	0.13
***m*FeP** (600 °C)	5	0.001	0.17
***p*FeP** (600 °C)	22	0.023	n.m.[a]

[a] n.m.: Not measured.

Also, we have added the following text in the revised manuscript:

*The porosity of **mFeP** and **pFeP** after annealing was characterized by gas adsorption technique, and the results are shown in Table S1. While N_2 adsorption indicates that both porphyrin molecules yielded poorly porous frameworks, CO_2 adsorption detects the presence of ultramicropores in **mFeP** annealed at 600 °C. Thus, the OCF includes a narrow space in which CO_2 can diffuse.*

Unfortunately, both ***m*FeP** and ***p*FeP** yield poorly porous frameworks. While N_2 adsorption rarely occur in both samples, CO_2 was adsorbed in ***m*FeP** annealed at 600 °C, indicating that this sample possess narrow pores which barely allow CO_2 diffusion. Since the both annealed samples derived from ***m*FeP** and ***p*FeP** are poorly porous, the discussion between the porosity and the electrochemical characterization is not meaningful very much. Moreover, to provide the electrochemical data on ***p*FeP**-derived samples, not small amount of experiments is necessary and it requires very long period, especially under the severe effect of the COVID-19. As explained in our answer to your comment #5, we have used three counterpart samples to discuss the effect of porphyrin-derived structure in the carbon framework, and the significance of the present OCF material has been already probed. However, as the

reviewer pointed out, the discussion about the porosity is important, and we have added the following discussion at the last paragraph of Results and Discussion:

The second problem is the not developed porosity. While the present OCFs possess narrow pores which barely allow CO_2 diffusion, the design of more developed porosity is expected to improve the electrocatalysis. These two problems could be solved by appropriate molecular design. Unlike the conventional carbonaceous catalysts, the OCF synthesis allows a precise molecular design based on the techniques of organic chemistry, and there is plenty of room for improvement [26]. For instance, introduction of a larger number of ethynyl groups to the porphyrin framework may be effective to form highly developed three-dimensional crosslinking and its translation into highly porous OCFs. The developed crosslinking is also expected to achieve an improved thermal stability of the framework, enabling higher annealing temperature to enhance the electric conductivity of OCFs. Such new tactics is under investigation.

To improve the poor porosity, a further new molecular design is necessary, and we are working on it now. We have we will be able to report the results in near future.

Catalysis Today
ITICAT2019

Guest Editors:
Asso. Prof. Cuijuan Zhang, Tianjin University, managing guest editor
Prof. Hisatomi Takashi, Shinshu University
Prof. Sibudjing Kawi, National University of Singapore
Prof. Fei Wei, Tsinghua University
Prof. Yongdan Li, Aalto University

A Letter of Invitation

Dear Dr. Nishihara,

Thanks for attending the Workshop on "Catalytic Reactions with Ion Transfer through Interfaces" in Aalto University, Finland. Associated with this workshop, a special issue of Catalysis Today entitled "SI: ITICAT2019" will be published.

On behalf of all the guest editors of the special issue, I am pleased to invite you to contribute one of your work to this special issue. Both reviews and full papers are welcome. You will find the guidelines for authors on the Catalysis Today homepage at https://www.elsevier.com/journals/catalysis-today/0920-5861/guide-for-authors.
Catalysis Today is a journal with its scope. A reasonable bias out of its scope but on the theme of this special issue is acceptable. You must select "**SI: ITICAT2019**" as the article type in the submission system.

Please kindly note that the full paper should be closely related to your presentation at ITICAT2019. The papers will be peer-reviewed as a standard submission and the decision will be made based only on their quality. The submission access will be available very soon. **The deadline for submission is December 31, 2019**. Early submission is highly appreciated. Please submit your manuscript with this invitation letter attached.

We look forward to hearing from you and receiving your manuscript.

Sincerely yours,

Cuijuan Zhang

Highlights

・The synthesis of iron-incorporated molecule-based ordered carbonaceous frameworks (OCFs) was achieved for the first time.

・The carbonization behavior and the structures of obtained OCFs were well analyzed by TG-MS, PXRD, XAFS, and HAADF-STEM.

・The introduction of ethynyl groups to the *meta*-positions of phenyl groups plays a crucial role for achieving OCFs.

・The OCFs with the conserved N_4-Fe coordination sphere enabled electrochemical reduction of CO_2 to CO.

Graphical Abstract

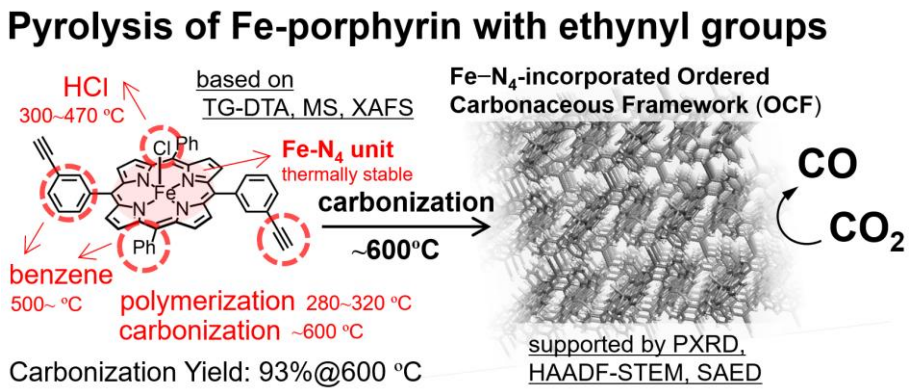

Iron porphyrin-derived ordered carbonaceous frameworks

Masanori Yamamoto[1], Kazuma Takahashi[1], Mao Ohwada[1], Yuxin Wu,[2] Kazuyuki Iwase[1,3], Yuichiro Hayasaka[4], Hisashi Konaka[5], Henry Cove[6], Devis Di Tommaso[6], Kazuhide Kamiya[2,3], Jun Maruyama[7], Fumito Tani[8], Hirotomo Nishihara[1,9]**

[1]*Institute of Multidisciplinary Research for Advanced Materials, Tohoku University, 2−1−1 Katahira, Aoba-ku, Sendai, Miyagi, 980−8577, Japan*

[2]*Graduate School of Engineering Science, Osaka University, 1−3 Machikaneyama, Toyonaka, Osaka 560−8531, Japan*

[3]*Research Center for Solar Energy Chemistry, Osaka University, 1-3 Machikaneyama, Toyonaka, Osaka 560−8531, Japan*

[4]*The Electron Microscopy Centre, Tohoku University, 2−1−1 Katahira, Aoba, Sendai 980−8577, Japan*

[5]*Application & Software Development Department, X-ray Instrument Division, Rigaku Corporation, 3−9−12, Matsubara-cho, Akishima-shi, Tokyo 196−8666, Japan*

[6]*School of Biological and Chemical Sciences, Queen Mary University of London, Mile End Road, E1 4NS London, United Kingdom*

[ˊ]*Research Division of Environmental Technology, Osaka Research Institute of Industrial Science and Technology, 1−6−50, Morinomiya, Jo-to-ku, Osaka 536−8553, Japan*

[8]*Institute for Materials Chemistry and Engineering, Kyushu University, Nishi-ku, Fukuoka 819−0395, Japan*

[9]*Advanced Institute for Materials Research (WPI-AIMR), Tohoku University, Katahira 2−1−1, Aoba-ku, Sendai, 980−8577, Japan*

*Corresponding author; Tel: +81-22-217-5625; Fax: +81-22-217-5626

E-mail: masanori.yamamoto.b2@tohoku.ac.jp; hirotomo.nishihara.b1@tohoku.ac.jp

Keywords:

Ordered carbonaceous frameworks; Iron porphyrin; CO_2 reduction; Carbon catalyst; XAFS

Abstract

Iron-incorporated ordered carbonaceous frameworks (OCFs) have been synthesized by the pyrolysis of iron porphyrin with ethynyl groups as polymerizable/carbonizable moieties at a temperature higher than 600 ºC. The pyrolysis behavior is analyzed by thermogravimetry-differential thermal analysis-mass spectrometry, and the obtained carbon materials are characterized by X-ray diffraction, X-ray absorption fine structure, and high-angle annular dark-field scanning transmission electron microscopy. The introduction of ethynyl groups at the *meta* positions of the peripheral phenyl groups is essential for efficient cross-linking upon thermal polymerization. The thermally stable polymer thus obtained can be transformed into OCFs with high carbonization yield of 93% at the subsequent carbonization. OCFs possess periodic structural regularity and porphyrin Fe-N_4 coordination structure, and exhibit electrocatalysis for the conversion of CO_2 into CO.

1. Introduction

Metal-incorporated carbonaceous materials have been subject to extensive studies because of their high catalytic ability and high stability [1-15]. They are usually prepared by a simple pyrolysis of organometallic substances including metal-organic-frameworks (MOF) [16] and porous organic polymers (POPs) [17, 18]. The conversion of poorly conductive MOFs and POPs to electrically conductive carbon materials has produced good catalysts. However, the resulting carbonaceous frameworks lose the structural ordering as well as the molecular-level fine chemical structures, and this makes it difficult to obtain the structure-activity relationship in their catalytic systems. Apart from the pyrolysis of organometallic complexes, the synthesis of nanocarbon materials with well-defined chemical structures have been achieved in C_{60} [19], nanocarbon molecules [20], single-walled carbon nanotubes [21], nano-graphenes [22, 23], and three-dimensional graphenes [24, 25]. Nevertheless, it has been difficult to achieve the precise and well-dispersed incorporation of metal centers to three-dimensionally ordered carbonaceous frameworks for catalysis [26]. In this regard, we have reported a new bottom-up method to prepare metal-incorporated ordered carbonaceous frameworks (OCFs) from Ni-based cyclic porphyrin dimer (**NiP**-dimer, Fig. 1) for efficient catalysis [27]. Thermally stable metalloporphyrins [28-30] are used as a building block, while diacetylene moieties function for the topochemical thermal polymerization to construct rigid three dimensional frameworks, enabling the structure retention upon the pyrolysis. More recently, we have synthesized OCFs also from Ni porphyrin with ethynyl groups as a thermally polymerizable moiety [31]. However, the metal center of the previous OCFs was limited to nickel [27, 31]. Moreover, the pyrolysis behavior of the ethynyl-incorporated porphyrin remained unclear with no guidance for molecular design. Herein we report the new OCFs derived from iron-containing porphyrins having two ethynyl groups with different substitutional manners (*m***FeP** and *p***FeP**, Fig. 1). The carbonization behavior was analyzed by thermogravimetry-differential thermal analysis-mass spectrometry (TG-DTA-MS), while the obtained carbon materials were characterized by powder X-ray diffraction (PXRD), X-ray absorption fine structure (XAFS), and high-angle annular dark-field scanning transmission electron microscopy (HAADF-STEM). These indicated that the ethynyl groups introduced to the *meta*-position of the peripheral phenyl groups play a crucial role for efficient linking and the carbonization to give OCFs. Finally, the

electrochemical reduction of CO_2 has been investigated using the OCFs and reference carbonaceous materials derived from tetraphenylporphyrin iron(III) chloride (**FeTPP**, Fig. 1). The importance of the initial association between reduced Fe species and CO_2 to the catalytic activity of these systems has been corroborated by means of density functional theory calculations.

2. Experimental

2.1. General

Solvents and chemicals were of reagent-grade quality, purchased commercially and used without further purification unless otherwise noted. All chemical reactions were performed under Ar unless otherwise noted. The structures of solvent-free powder crystals were analyzed by synchrotron PXRD (SPring-8 BL19B2, 0.61992 Å) by the method reported in the literature [27].

2.2. Synthesis

^{1}H nuclear magnetic resonance (NMR) spectra were recorded on a JEOL ECS400 (400 MHz) spectrometer in $CDCl_3$. Chemical shifts have been reported in δ ppm units with reference to an internal standard of tetramethylsilane ($Si(CH_3)_4$; 0.00 ppm) and the internal residual solvent peak ($CHCl_3$; 7.26 ppm) according to the literature [32]. Silica gel column chromatography was performed using neutral Silica Gel 60 (Nacalai tesque, average size of the particle: 75 μm). Thin layer chromatography (TLC) was conducted on aluminum plates coated with silica gel 60 F254 (Merck). Steady-state absorption spectra were measured with a Shimadzu UV-mini spectrometer with a data interval of 1.0 nm. These spectra were taken with ca. 10^{-5}–10^{-6} M solutions in a quartz cell with a path length of 1 cm. High resolution matrix-assisted laser desorption/ionization (MALDI) mass spectrometry was conducted on a solariX-TOH1 9.4T (Bruker Daltonics Inc.) with tetraphenylbutadiene as a matrix. ***m*FeP** was synthesized by the acid-catalyzed annulation of 3-(trimethylsilylacetyl)benzaldehyde [33] and phenyldipyrromethane [34] using boron trifluoride etherate followed by the incorporation of iron to the center of the tetrapyrrolic macrocycle (***m*H$_2$P**) and the removal of the trimethylsilyl protecting groups [35] in the sequential three steps, and they were characterized by MS, UV-Vis, and ^{1}H NMR (if possible). ***p*FeP** was synthesized according to the literature [36].

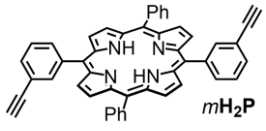

3-(Trimethylsilylethynyl)benzaldehyde (0.80 g, 4.0 mmol), phenyldipyrromethane (0.89 g, 4.0 mmol), NH_4Cl (2.1 g, 40 mmol), acetonitrile (400 mL) and BF_3•OEt_2 (50 μL, 0.4 mmol) were added into a round-bottomed flask, and the mixture was stirred under N_2 at 0 °C for 4 h in the dark. 2,3-dichloro-5,6-dicyano-*p*-benzoquinone (DDQ, 1.8 g, 8.0 mmol) was then added to the solution and stirred for 2 h. After the addition of triethylamine (110 μL, 0.8 mmol), the solution was evaporated. The residue was purified by alumina column chromatography followed by silica gel column chromatography

using dichloromethane as a solvent. Then, the solution was evaporated, and the residue was purified by silica gel column chromatography again (hexane/dichloromethane = 3/1). After the purification, the solution was evaporated to give the free base porphyrin (***m*H$_2$P**) as a red powder (105 mg, 130 μmol, 6.5%) after vacuum dried at 40 °C.

^{1}H NMR ($CDCl_3$, 500 MHz): δ (ppm) = 8.86 (d, 4H, J = 6.0 Hz), 8.82 (d, 4H, J = 6.0 Hz), 8.34 (s, 2H), 8.22 (d, 4H, J = 2.0 Hz), 8.20 (d, 2H, J = 2.5 Hz), 7.90 (d, 2H, J = 10.0 Hz), 7.79 (d, 2H, J = 6.0 Hz), 7.76 (t, 4H, J = 10.0 Hz), 7.69 (t, 2H, J = 19.0 Hz), 0.27 (s, 18H), −2.82 (s, 2H).

MS (*maldi-tof*, dithranol+$CHCl_3$): *m/z* calcd for $C_{54}H_{46}N_4Si_2^+$: 806.3, found: 807.1.

UV-Vis ($CHCl_3$): λ_{max} (ε) = 420 (473 000), 515 (19 500), 550 (7 800), 590 (6 200), 645 nm (400 M^{-1} cm^{-1}).

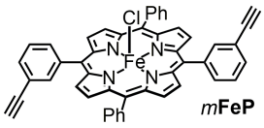

***m*FeP**

To a round-bottomed flask equipped with a reflux condenser were added free base porphyrin (170 mg, 0.21 mmol), $FeBr_2$ (453 mg, 2.1 mmol), toluene (200 mL), methanol (35 mL), and 2,6-lutidine (450 μL, 4.0 mmol). The mixture was refluxed under Ar at 105 °C for overnight. Then, the mixture was dissolved in toluene and washed with HCl (1 mol L^{-1}) several times. The organic phase was separated, dried over Na_2SO_4, filtered, and evaporated to give the intermediate product. The crude material was then dissolved in tetrahydrofuran (THF, 65 mL), and tetrabutylammonium fluoride (TBAF, 1 mol L^{-1}, 0.70 mL, 0.70 mmol) was added to the solution. After stirring at room temperature under Ar for 7 h, toluene was added to the solution, and washed with HCl (1 mol L^{-1}). The organic layer was separated, dried over Na_2SO_4, filtered, and evaporated. The residue was purified by column chromatography (hexane/dichloromethane = 96/4), and recrystallized from methanol and sat. aqueous NaCl solution to give a dark brown powder quantitatively after vacuum dried at 40 °C.

HRMS (*maldi-tof*, tetraphenylbutadiene+$CHCl_3$): *m/z* calcd for $C_{48}H_{28}ClN_4Fe^+$: 751.1346, found: 751.1347.

UV-Vis ($CHCl_3$): λ_{max} (ε) = 417 (108 000), 510 (13 400), 579 (3 500), 660 (2 800), 695 nm (2 900 M^{-1} cm^{-1}).

The pyrolysis behaviors of porphyrins were analyzed by thermogravimetry (TG) coupled with differential thermal analysis (DTA) on a thermogravimeter (Netzsch, STA2500) from 25 to 600 ºC at 10 ºC min^{-1} under a steady flow of He at 50 mL min^{-1}. The effluent gas from the TG-DTA was analyzed using a quadrupole mass spectrometer (JEOL, JMS-Q1500GC). Heat treatment of ***m*FeP** and ***p*FeP**, was performed at a heating rate of 10 ºC min^{-1} ramped at a designed temperature under a steady flow of N_2 (288 mL min^{-1}) using a tubular furnace. In the cases of 450, 600, and 700 ºC, heating was stopped immediately when the temperature reached the designated value. In the case of 270 ºC, the temperature was maintained at the target temperatures for 1 h. As a reference, **FeTPP** (≥94%, Sigma-Aldrich) was carbonized at 600 or 700 ºC by the same manner.

2.3. Analysis

PXRD patterns of the samples were recorded with an X-ray diffractometer (Rigaku, MiniFlex 300/600) with Cu Kα radiation (λ = 1.5418 Å) generated at 40 kV and 15 mA. The morphology of the samples was analyzed

using field emission-scanning electron microscopy (FE-SEM, Hitachi S-4800). HAADF-STEM, the selected area electron diffraction (SAED), and the energy-dispersive X-ray spectrometry (EDS)-mapping of materials were conducted on a transmission electron microscope (ThermoScientific Titan^3 60-300 Double Corrector, FEI-Company) equipped with an energy-dispersive X-ray spectrometer (Super-X) at an acceleration voltage of 200 kV. The XAFS of the Fe–K edge (~7115 eV) was analyzed by synchrotron X-ray absorption spectroscopy, and the obtained data was analyzed using REX2000 (Rigaku). EXAFS was analyzed with k-weight of 3. N_2 and CO_2 adsorption isotherms were measured at –196 °C and 25 °C, respectively on MicrotrocBEL BELMAX. From the N_2 adsorption isotherm, the specific surface area was calculated by the Brunauer–Emmett–Teller (BET) method in the pressure range of P/P_0 = 0.05–0.35. The total pore volume (V_{N2}) was calculated at P/P_0 = 0.96. From the CO_2 adsorption isotherm, the pore volume (V_{CO2}) was calculated by the Duinin–Radushkevich equation.

2.4. Electrochemistry

The activities of the annealed ***m*FeP** and reference samples for electrochemical reduction of CO_2 were evaluated based on the method previously established [37]. Briefly, 0.6 mg of each sample was mixed with 28.5 μL of Nafion solution (5%, Du Point, Corp.) dissolved with 300 μL of ultra-pure water, and the mixture was sonicated for 30 min to form a catalyst ink. 60 μL of the catalyst ink was then dropped on a glassy carbon plate (2 cm^2) to fabricate a working electrode composed of catalyst layer. Prior to casting the catalyst ink, a GC electrode was sequentially polished with 1.00 and 0.05 μm aluminum suspensions. No conductive additive was used to evaluate the effect of sample conductivity. Electrochemical measurements including controlled-potential electrolysis were performed on an electrochemical measurement system (HZ-5000, Hokuto Denko) at room temperature using a three-electrode cell with two compartments (*vide infra*). Cation-exchange membrane (Nafion, Sigma-Aldrich) was used to separate the working compartment and the counter compartment. The supporting electrolyte was prepared using $KHCO_3$ (99.7%, Sigma-Aldrich). A Pt wire was used as a counter electrode, and a Ag/AgCl (sat. KCl aqueous solution) was used as a reference electrode. The volumes of catholyte and gas phase are 13 and 4.4 ml, respectively, in the three-electrode cell. The measured potentials were recorded with respect to the Ag/AgCl reference electrode, and they were converted to the potential versus reversible hydrogen electrode (RHE) using the following relationship:

$$E_{RHE} = E_{Ag/AgCl} + 0.199 + 0.0591 \times pH \text{ / V versus RHE}$$

Cyclic voltammetry was performed in 0.1 M phosphate buffer saturated with Ar and in 0.1 M $KHCO_3$ saturated with CO_2 (pH 6.8). The latter was prepared by the introduction of CO_2 gas (>99.5% purity) to the compartments for more than 30 min. CO_2 reduction reaction was examined in the 0.1 M $KHCO_3$ electrolyte. The headspace gas was introduced to gas chromatograph (GC) system using a gas-tight syringe and the gas products were quantitatively analyzed using a gas chromatography-mass spectrometer (GCMS-QP 2010 Plus, Shimadzu Corporation) with a Micropacked-ST MP-01 column (shincarbon-ST 80/100 mesh, Shinwa Chemical Industries

Ltd.) as a stationary phase. He gas was used as a mobile phase. Liquid phase products were quantified using ^{1}H NMR with 0.55 μmol of dimethyl sulfoxide (DMSO) as an internal standard, and the chemical shifts were referenced to the literature. The Faraday efficiency (FE) of the hydrocarbon products was calculated with the number of electrons required for the formation of the products: Reduction of CO_2 into CO required $2e^-/2H^+$.

2.5. Quantum chemical calculations

We have conducted density functional theory (DFT) calculations to determine the reaction energy diagram for the electrochemical reduction of CO_2 on the iron porphine [FeP] complex (the simplest porphyrin ligand). DFT calculations have been performed with the Gaussian program (G09 D01) [38]. The unrestricted version of the Becke, 3-parameter, Lee–Yang–Parr [39] functional (UB3LYP) was used for the exchange and correlation terms, together with Grimme's general dispersion correction D3 [40]. The triple-ζ 6−311+G(d,p) basis set was used for all atoms. All calculations (geometry optimization and frequencies) were conducted with the continuum polarized conductor model (CPCM) [41] to account for the solvation effects (water). The combination of B3LYP with a basis set of triple-ζ quality and solvent corrections give bond energies that appear to agree well with experiment [42, 43]. Iron porphyrin can appear in a range of low-energy, close-lying spin states [44]. Therefore, the low-energy pathways for the electrochemical reduction of CO_2 to CO on [FeP] were determined by optimizing the geometries of each individual iron-porphyrin compound in the reaction, in all available spin states, and by then computing the reaction energy between the lowest energy states. Full details of the spin energetics are given in Supporting Information.

3. Results and Discussion

The molecules were synthesized and characterized by the steady-state absorption spectroscopy: Molar extinction coefficients (ε) of ***m*H$_2$P** and ***m*FeP** for the Soret bands were 473,000 M^{-1} cm^{-1} and 108,000 M^{-1} cm^{-1}, respectively. These values are in a good agreement with those reported for the similar structures [45]. The HRMS of ***m*FeP** also supported the successful synthesis of the molecule (Fig. S1). After the crystallization from methanol and sat. aqueous NaCl solution, a dark brown crystal was obtained for ***m*FeP**. The pyrolysis behaviors of ***p*FeP** [36] and ***m*FeP** crystals were then investigated under a steady flow of inert gas by TG-DTA-MS in the temperature range between 25 ºC and 800 ºC (Fig. 2). In Fig. 2a, ***m*FeP** shows an exothermic peak at 305 °C, corresponding to thermal polymerization of ethynyl groups [31]. The polymerization behavior was confirmed by dissolution of unreacted monomer on ***m*FeP**: While the dissolution of unreacted monomer was observed in ***m*FeP** heat-treated at 270 °C (below the DTA peak temperature), no monomer dissolution was confirmed when heated at 450 °C (Fig. S2). Note that thermal polymerization of ethynyl groups is not associated with weight decrease nor desorption of chemical species [31]. In Fig. 2b, HCl desorption was observed at 300–480 °C. Based on the molecular weight of ***m*FeP** and the weight decrease (5%) at the temperature range, almost quantitative elimination of the chloride atom as HCl was expected from the framework. The weight was again decreased by 4% at

around 540−700 ºC with the desorption of benzene (*m/z* = 78) and tolyl radical (*m/z* = 91). The weight change corresponded to ~10% of desorption of the peripheral aryl groups. Overall, the sample weight was gradually decreased upon heating, and reached 93% at 600 ºC and 90% at 700 ºC. There was no pyrrole (*m/z* = 67) detected, and this supported the high thermal stability of the metalloporphyrin center [27, 31]. On the contrary, H_2 (*m/z* = 2) and C_2H_4 (*m/z* = 28) were detected at the temperature higher than 600 ºC. Although we cannot exclude the possibility that the peak of *m/z* = 28 may come from N_2, these gas evolution can be explained by the carbonization and the elimination of ethynyl units at the temperature. For ***p*FeP** (Fig. 2c,d), small weight decrease around 200 °C is ascribed to desorption of remaining solvents. The overall pyrolysis behavior of ***p*FeP** is similar to that of ***m*FeP**, and almost all of chloride atoms were desorbed as HCl. However, there is a noticeable difference in the polymerization step. An intense exothermic peak corresponding to thermal polymerization appeared at 350 ºC, slightly higher than that of ***m*FeP**. Moreover, the area of the peak was 1.4 times smaller than that of ***m*FeP.** Since the effect of HCl desorption to the DTA data should be even in both samples, this implies the less efficient polymerization of the ethynyl linking units for ***p*FeP**, and this is supported by the significant evolution of C_2H_4 at higher temperature (>600 ºC) in ***p*FeP**.

The resulting products after the pyrolysis at the specified temperature were then analyzed by FE-SEM and PXRD. The SEM images of the pristine and the annealed ***m*FeP** (Fig. S3) have similar appearance, indicating that the pyrolysis took place with the grain shape well retained even after the carbonization. As shown in Fig. 3a, the PXRD pattern of pristine ***m*FeP** showed the peaks at 2θ = 8.4 (1.0 nm) and 10.8º (0.80 nm). After the thermal treatment at 600 ºC, ***m*FeP** mantained the PXRD peaks at 2θ = 8.0 (1.1 nm) and 10.2º (0.85 nm). This is in a stark contrast to ***p*FeP** where no peak was observed after the pyrolysis (Fig. 3b). Thus, the introduction of ethynyl groups into *meta*-position of the peripheral phenyl groups is more suitable for an efficient cross-linking upon the thermal treatment as well as the retention of the periodic regularity than the *para*-substitutions. The periodicity in ***m*FeP** annealed at 600 °C was further corroborated by HAADF-STEM (Fig. 3c) and SAED (Fig. 3d), showing a lattice spacing of 1.2 nm. In the HAADF-STEM image, heavier atoms appear as white contrast, and Fig. 3c and 3d indicate that Fe atoms are arrayed with the periodicity of 1.2 nm.

Thus, ***m*FeP** yields the OCF, while ***p*FeP** produces the disordered carbon material. The difference can be rationalized by the freedom of rotation of the peripheral substituents: *m*-Ethynyl substituted phenyl groups have considerable freedom of rotation, enabling the thermal polymerization of the adjacent triple bonds to give the robust frameworks, while *p*-substituted ethynyl groups have low probability of the linking owing to the lower freedom of rotation. For confirming this, the atomic configuration of ***m*FeP** in the crystal was then analyzed. Fig. 4 shows the crystal structure of ***m*FeP** solved by synchrotron PXRD analysis (Fig. S4). The distance between the adjacent ethynyl groups is 0.37 nm so the thermal linkage could be indeed feasible after the rotation of the phenyl groups, although the dislocation of molecules may be required. The porosity of ***m*FeP** and ***p*FeP** after annealing was characterized by gas adsorption technique, and the results are shown in Table S1. While N_2 adsorption indicates that both porphyrin molecules yielded poorly porous frameworks, CO_2 adsorption detects the presence of ultramicropores in ***m*FeP** annealed at 600 °C. Thus, the OCF includes a narrow space in which CO_2 can diffuse.

Next, we examined the local atomic structures of the Fe-centered macrocyclic cores in *m***FeP** via the XAFS analysis of the original molecular crystals and the derived materials annealed at the specified temperatures. Fe K-edge X-ray absorption near-edge structure (XANES) of all *m***FeP** derivatives (Fig. 5a) exhibits similar shape, indicating that the oxidation states and the spin states of the Fe center are kept with tetrapyrrole-coordinated Fe site. All the spectra showed a characteristic peak at 7113 eV, and this could be the fingerprint of the square planar Fe−N_4 structure with the 1 s to 4p_z transition [46]. This is in a sharp contrast to **FeTPP** annealed at 600 ºC, where the shoulder peak was seldom recognized (Fig. 5a, dashed line). This supported the importance of the ethynyl groups for efficient linking to maintain the Fe−N_4 coordination sphere. The local environment surrounding Fe was further analyzed by the extended X-ray absorption fine structure (EXAFS). For all the samples, the 1st peak of the pseudo-radial structural functions showed similar shape as well as position except for the intensity. Because they differ from Fe metal, oxides, and carbides that has been typically reported to form after the carbonization of porphyrins, we can conclude here that the obtained carbon materials maintains the tetrapyrrole structure where iron center is coordinated by the four pyrrolic nitrogen atoms even after the pyrolysis. This was supported by the well-dispersed C, N, and Fe atoms as confirmed by HAADF-STEM/EDS analysis of *m***FeP** annealed at 600 ºC (Fig. S5). From the TG-DTA-MS analysis (Fig. 2a and b), Cl atom was desorbed from Fe center at 300 ºC. Nevertheless, XANES and EXAFS of all *m***FeP** derivatives showed similar shape except for the intensity in the EXAFS, indicating the oxidation state of the metal center to be Fe^{III}. The decrease in the intensity of EXAFS upon the heating could be explained by the desorption of heavy Cl atoms with large X-ray scattering from the coordination sphere as well as the increase in the Debye-Waller factor upon the carbonization. On the other hand, the 2nd peak position of *m***FeP** is shifted to longer distance with increasing the annealing temperature, and this can be ascribed to the structure change of the porphyrin framework into carbonaceous framework.

The pyrolysis behavior was summarized in Fig. 6. The polymerization of the ethynyl units in *m***FeP** gave rigid cross-linking, and the pyrolysis of *m***FeP** yielded an OCF with a periodicity of 1.1 nm (2θ = 8.0º) after the carbonization at 600 ºC as confirmed by PXRD, HAADF-STEM, and SAED, while the thermal treatment of *p***FeP** did not give an ordered structure. For the pyrolysis behavior, HCl gas with *m/z* of 36 and 38 was recognized by MS when heated to 300 ºC, and the TG supported the dissociation of Fe−Cl bond and the quantitative release of HCl from the architecture. At the temperature higher than 500 ºC, benzene and tolyl radical with *m/z* of 78 and 91 were detected, indicating the elimination of the peripheral aromatic units. When the temperature reached to 600 ºC, ethylene (*m/z* = 28) and hydrogen (*m/z* = 2) were detected with the significant heat, indicating the carbonization and the partial degradation of the molecular structure at the temperature. The carbonization proceeded with the excellent yield of 93% at 600 ºC, and this matched well with the evolution of HCl and the partial elimination of aromatic rings while the core π-system maintained. As there was almost no pyrrole (*m/z* = 67) detected, the tetrapyrrole skeleton should be maintained after the carbonization. This explanation is in a good agreement with the XAFS, where the squarely tetra-coordinated Fe−N_4 structure was confirmed even after the pyrolysis.

With the well-dispersed Fe center within the ordered and linked carbon frameworks, we then investigated the electrocatalytic CO_2 reduction reactions (CO_2RRs). The basic electrocatalytic behaviors of *m***FeP** annealed at 600 and 700 °C were examined by cyclic voltammetry with and without the presence of CO_2 (Fig. S6). For compari-

son, **FeTTP** annealed at 600 and 700 °C were also investigated. Without the presence of CO_2, all the samples showed current increase below –0.8 V due to hydrogen evolution reactions. Only in ***m*FeP** annealed at 600 °C, current decrease was observed around –0.9 to –1.5 V when CO_2 was introduced. A possible reason for the current decrease is the occurrence of CO_2RRs on the same catalytic sites which were used for hydrogen evolution reactions, and additionally, the activity of CO_2RRs is not significantly high. However, detail discussion is difficult only using the cyclic voltammograms. Thus, the CO_2RRs investigation was carried out at a constant potential using 0.1 M aqueous $KHCO_3$ solution (pH = 6.8) in the presence of saturated CO_2 gas. The liquid phase analysis by NMR showed almost no formation of formate, while CO was detected in the gas phase when the potential is more negative than −0.6 V versus reversible hydrogen electrode (RHE), and the Faraday efficiency (FE) reached 30% at −1.0 V versus RHE when 600 ºC-annealed ***m*FeP** was used as a catalyst (Fig. 7a). This value is five times higher than the FE obtained with **FeTPP** annealed at the same temperature. This could be attributed to the well-retained Fe−N_4 coordination sphere for 600 ºC-annealed ***m*FeP** as compared with the corresponding **FeTPP** material (Fig. 5a). With *meta*-ethynyl substitution on the peripheral phenyl groups, the efficient linking of molecules was achieved upon the pyrolysis; this could provide a well-conserved Fe-N_4 catalytic center as well as a pathway for efficient electron conveyance. The CO_2RRs were performed also on ***m*FeP** and **FeTPP** annealed at 700 °C. All the results were summarized in Table S2-5. As shown in Fig. S7 and S8, the major products are CO and H_2 for all the samples, and only a trace amount of CH_4 was detected, which coincides with the results of CO_2RR by the reported Fe-based catalysts [5,47]. While Ni-based OCF synthesized at 600 °C can achieve a good CO_2RR catalysis [31], higher annealing temperature of 700 °C provides better electric conductivity [27] which is preferable for superior performance. However, ***m*FeP** annealed at 700 °C without ordered structure (Fig. 3a) showed much lower activity for CO_2RRs compared to the sample annealed at 600 °C. This also indicates the significance of the porphyrin-structure retention for the CO_2RRs activity.

One of the key factors underlying the catalytic performance of electrocatalysts for CO_2 reduction is the interaction between the adsorbate and the metal-organic complex [48]. Therefore, in order to understand the effect of the oxidation state of the Fe center on the electrochemical conversion of CO_2 to CO, we have conducted DFT calculations of the mechanism of CO_2 reduction catalysed by iron porphine [FeP] with the CO_2 adsorption taking placing on the following three complexes: the doubly negative $[FeP]^{-2}$, the singly negative $[FeP]^{-}$, and the neutral $[FeP]^{0}$ (see Supporting Information and Table S6). Simulations showed that the Fe porphine-CO_2 complex is thermodynamically unfavoured starting from $[FeP]^{0}$ and $[FeP]^{-}$ (Fig. 7b). Thus, the coordination of CO_2 to $[FeP]^{0}$ and $[FeP]^{-}$ will be rather uphill and less feasible, and this could lead to H_2 evolution to be kinetically dominant. Fig. 7b shows that initial step of CO_2 conversion to *COOH could be further inhibited by the weak COOH binding to the $[FeP]^{0}$. On the contrary, the more favourable association of CO_2 (1 $kJ.mol^{-1}$) and strong stabilization of *COOH on the $[FeP]^{2-}$ complex (-64 $kJ\ mol^{-1}$) suggest that higher Faraday efficiencies could be achieved under electrochemical conditions promoting well-reduced Fe species (Table S7). Because in aqueous solutions, there is a higher concentration of bicarbonate (HCO_3^-) than CO_2, we have also computed the interaction of HCO_3^- with the iron porphine complexes. The (free) energies of adsorption of HCO_3^- on $[FeP]^{0}$, $[FeP]^{-}$ and $[FeP]^{2-}$ are marginally endergonic ($\Delta G > 0$) and similar in value to the values computed for the CO_2 molecule (Table S8). In the

initial process of CO_2 binding to the active site of the catalyst, there could be some competition with the bicarbonate molecule.

As described above, experiments and simulations have demonstrated that embedding the Fe-N_4 coordination structure in a conductive carbon framework is crucial to achieve electrocatalysis for CO_2 reduction. At the same time, two problems have emerged regarding effective CO_2 conversion. One of them is not sufficient electric conductivity of OCF annealed at 600 °C. The calculations demonstrated thermodynamically favored catalysis on well-reduced Fe sites, while less-reduced Fe sites cause hydrogen evolution. The lack of electric conductivity thus causes low FE in electrochemical CO_2 conversion. To improve the electric conductivity, application of higher annealing temperature is effective [27], whereas the fine chemical structure of ***m*FeP** collapses at 700 °C, resulting in very low FE (Table S3). To overcome this problem, it is necessary to improve the thermal stability of crystalline polymer which is formed as an intermediate of OCF. The second problem is the not developed porosity. While the present OCFs possess narrow pores which barely allow CO_2 diffusion, the design of more developed porosity is expected to improve the electrocatalysis. These two problems could be solved by appropriate molecular design. Unlike the conventional carbonaceous catalysts, the OCF synthesis allows a precise molecular design based on the techniques of organic chemistry, and there is plenty of room for improvement [26]. For instance, introduction of a larger number of ethynyl groups to the porphyrin framework may be effective to form highly developed three-dimensional crosslinking and its translation into highly porous OCFs. The developed crosslinking is also expected to achieve an improved thermal stability of the framework, enabling higher annealing temperature to enhance the electric conductivity of OCFs. Such new tactics is under investigation.

4. Conclusions

Ordered carbonaceous frameworks (OCFs) with tetrapyrrole-coordinated Fe sites have been prepared for the first time. The carbonization proceeded in high yield, and the porphyrin-derived Fe center was well distributed over the nanostructured framework as confirmed by XAFS and HAADF-STEM/EDS analyses. It is found that the introduction of ethynyl groups to *meta*-position of the peripheral phenyl groups of porphyrins is important for efficient crosslinking between molecules and the subsequent carbonization for OCFs, while the *para*-substituted molecule gave disordered carbonaceous products. The prepared OCFs achieved an efficient electrochemical reduction of CO_2 as compared with the reference systems lacking the tetrapyrrole-coordinated Fe sites, and calculation supported the importance of the initial adsorption of CO_2 to the well-reduced Fe sites for efficient electrochemical reduction of CO_2 over H_2 evolution. The findings for molecular design where *m*-ethynylphenyl groups are important to obtain OCFs will be an important guideline for the development of a variety of metal-incorporated OCF materials in future for efficient catalysis.

Acknowledgements

This work was supported by JST CREST Grant Number JPMJCR18R3; JSPS KAKENHI Grant Number 19K15281; and the Cooperative Research Program for CORE lab of "Five-star Alliance" in "NJRC Mater. & Dev." The synchrotron radiation experiments were performed at SPring-8 with the approval of the Japan Synchrotron Radiation Research Institute (JASRI, proposal no. 2019A1617; 2019B1159). We thank Prof. T. Kyotani for his advice, and Tohoku University Molecule and Material Synthesis Platform in Nanotechnology Platform Project for HRMS analysis operated by Dr. Hiroyuki Momma. We are grateful to the UK Materials and Molecular Modelling Hub for computational resources, which is partially funded by EPSRC (EP/P020194/1). This research utilized Queen Mary's Apocrita HPC facility, supported by QMUL Research-IT. http://doi.org/10.5281/zenodo.438045.

Appendix A. Supplementary data

Supplementary data associated with this article can be found, in the online version, at doi:10.1016/j.cattod.2020.##.###

References

[1] J. Gu, C.-S. Hsu, L. Bai, H.M. Chen, X. Hu, Science 364 (2019) 1091-1094.

[2] B.Y. Xia, Y. Yan, N. Li, H.B. Wu, X.W. Lou, X. Wang, Nat. Energy 1 (2016) 15006.

[3] L. Han, X. Liu, J. Chen, R. Lin, H. Liu, F. Lu, S. Bak, Z. Liang, S. Zhao, E. Stavitski, J. Luo, R.R. Adzic, H.L. Xin, Angew. Chem. Int. Ed. 58 (2019) 2321-2325.

[4] X. Wang, Z. Ma, L. Chai, L. Xu, Z. Zhu, Y. Hu, J. Qian, S. Huang, Carbon 141 (2019) 643-651.

[5] T.N. Huan, N. Ranjbar, G. Rousse, M. Sougrati, A. Zitolo, V. Mougel, F. Jaouen, M. Fontecave, ACS Catal. 7 (2017) 1520-1525.

[6] P. Cao, Y. Liu, X. Quan, J. Zhao, S. Chen, H. Yu, Catal. Today 327 (2019) 366-373.

[7] D.M. Koshy, S. Chen, D.U. Lee, M.B. Stevens, A.M. Abdellah, S.M. Dull, G. Chen, D. Nordlund, A. Gallo, C. Hahn, D.C. Higgins, Z. Bao, T.F. Jaramillo, Angew. Chem. Int. Ed. 59 (2020) 4043-4050.

[8] J. Maruyama, T. Amano, S. Inoue, Y. Muramatsu, N. Yoshizawa, E.M. Gullikson, Chem. Commun. 54 (2018) 8995-8998.

[9] P. Ling, Q. Hao, J. Lei, H. Ju, J. Mater. Chem. B 3 (2015) 1335-1341.

[10] S. Brüller, H.-W. Liang, U.I. Kramm, J.W. Krumpfer, X. Feng, K. Müllen, J. Mater. Chem. A 3 (2015) 23799-23808.

[11] H.-W. Liang, X. Zhuang, S. Brüller, X. Feng, K. Müllen, Nat. Commun. 5 (2014) 4973.

[12] P. Su, K. Iwase, T. Harada, K. Kamiya, S. Nakanishi, Chem. Sci. 9 (2018) 3941-3947.

[13] H. Fei, J. Dong, D. Chen, T. Hu, X. Duan, I. Shakir, Y. Huang, X. Duan, Chem. Soc. Rev. 48 (2019) 5207-5241.

[14] Y. Ouyang, L. Shi, X. Bai, Q. Li, J. Wang, Chem. Sci. 11 (2020) 1807-1813.

[15] C. Ban, S. Yang, H. Kim, D.H. Kim, Catal. Today 352 (2020) 66-72.
[16] C. Wang, J. Kim, J. Tang, J. Na, Y.-M. Kang, M. Kim, H. Lim, Y. Bando, J. Li, Y. Yamauchi, Angew. Chem. Int. Ed. 59 (2020) 2066-2070.
[17] Q. Lin, X. Bu, A. Kong, C. Mao, F. Bu, P. Feng, Adv. Mater. 27 (2015) 3431-3436.
[18] G. Lu, Y. Zhu, K. Xu, Y. Jin, Z.J. Ren, Z. Liu, W. Zhang, Nanoscale 7 (2015) 18271-18277.
[19] G. Otero, G. Biddau, C. Sanchez-Sanchez, R. Caillard, M.F. Lopez, C. Rogero, F.J. Palomares, N. Cabello, M.A. Basanta, J. Ortega, J. Mendez, A.M. Echavarren, R. Perez, B. Gomez-Lor, J.A. Martin-Gago, Nature 454 (2008) 865-868.
[20] Y. Segawa, H. Ito, K. Itami, Nat. Rev. Mater. 1 (2016) 15002.
[21] H. Omachi, T. Nakayama, E. Takahashi, Y. Segawa, K. Itami, Nat. Chem. 5 (2013) 572-576.
[22] K. Kawasumi, Q. Zhang, Y. Segawa, L.T. Scott, K. Itami, Nat. Chem. 5 (2013) 739-744.
[23] Y. Yano, N. Mitoma, K. Matsushima, F. Wang, K. Matsui, A. Takakura, Y. Miyauchi, H. Ito, K. Itami, Nature 571 (2019) 387-392.
[24] H. Nishihara, T. Kyotani, Chem. Commun. 54 (2018) 5648-5673.
[25] H. Nishihara, H. Fujimoto, H. Itoi, K. Nomura, H. Tanaka, M.T. Miyahara, P.A. Bonnaud, R. Miura, A. Suzuki, N. Miyamoto, N. Hatakeyama, A. Miyamoto, K. Ikeda, T. Otomo, T. Kyotani, Carbon 129 (2018) 854-862.
[26] S. Fa, M. Yamamoto, H. Nishihara, R. Sakamoto, K. Kamiya, Y. Nishina, T. Ogoshi, Chem. Sci. 11 (2020) 5866-5873.
[27] H. Nishihara, T. Hirota, K. Matsuura, M. Ohwada, N. Hoshino, T. Akutagawa, T. Higuchi, H. Jinnai, Y. Koseki, H. Kasai, Y. Matsuo, J. Maruyama, Y. Hayasaka, H. Konaka, Y. Yamada, S. Yamaguchi, K. Kamiya, T. Kamimura, H. Nobukuni, F. Tani, Nat. Commun. 8 (2017) 109.
[28] J.-H. Chou, M.E. Kosal, H.S. Nalwa, N.A. Rakow, K.S. Suslick, The Porphyrin Handbook: Applications of Porphyrins and Metalloporphyrins to Materials Chemistry (Eds: K. M. Kadish, K. M. Smith, G. Roger), Academic Press, 2000.
[29] K. Kalyanasundaram, Photochemistry of polypyridine and porphyrin complexes, Academic Press, London; San Diego, 1992.
[30] R.-J. Niu, W.-F. Zhou, Y. Liu, J.-Y. Yang, W.-H. Zhang, J.-P. Lang, D.J. Young, Chem. Commun. 55 (2019) 4873-4876.
[31] H. Nishihara, K. Matsuura, M. Ohwada, M. Yamamoto, Y. Matsuo, J. Maruyama, Y. Hayasaka, S. Yamaguchi, K. Kamiya, H. Konaka, M. Inoue, F. Tani, Chem. Lett. 49 (2020) 619-623.
[32] G.R. Fulmer, A.J.M. Miller, N.H. Sherden, H.E. Gottlieb, A. Nudelman, B.M. Stoltz, J.E. Bercaw, K.I. Goldberg, Organometallics 29 (2010) 2176−2179.
[33] W.B. Austin, N. Bilow, W.J. Kelleghan, K.S.Y. Lau, J. Org. Chem. 46 (1981) 2280-2286.
[34] F. Matino, G. Schull, U. Jana, F. Kohler, R. Berndt, R. Herges, Chem. Commun. 46 (2010) 6780-6782.
[35] P.G.M. Wuts, T.W. Greene, Protective Groups in Organic Synthesis, Wiley-Interscience, Hoboken, NJ, 2007.

[36] Q. Dong, W. Qu, W. Liang, F. Tai, K. Guo, C.-W. Leung, Y.H. Lo, W.-Y. Wong, J. Mater. Chem. C 4 (2016) 5010-5018.
[37] P. Su, K. Iwase, S. Nakanishi, K. Hashimoto, K. Kamiya, Small 12 (2016) 6083-6089.
[38] M.J. Frisch, G.W. Trucks, H.B. Schlegel, G.E. Scuseria, M.A. Robb, J.R. Cheeseman, G. Scalmani, V. Barone, B. Mennucci, G.A. Petersson, H. Nakatsuji, M. Caricato, X. Li, H.P. Hratchian, A.F. Izmaylov, J. Bloino, G. Zheng, J.L. Sonnenberg, M. Hada, M. Ehara, K. Toyota, R. Fukuda, J. Hasegawa, M. Ishida, T. Nakajima, Y. Honda, O. Kitao, H. Nakai, T. Vreven, J.A. Montgomery Jr., J.E. Peralta, F. Ogliaro, M. Bearpark, J.J. Heyd, E. Brothers, K.N. Kudin, V.N. Staroverov, R. Kobayashi, J. Normand, K. Raghavachari, A. Rendell, J.C. Burant, S.S. Iyengar, J. Tomasi, M. Cossi, N. Rega, J.M. Millam, M. Klene, J.E. Knox, J.B. Cross, V. Bakken, C. Adamo, J. Jaramillo, R. Gomperts, R.E. Stratmann, O. Yazyev, A.J. Austin, R. Cammi, C. Pomelli, J.W. Ochterski, R.L. Martin, K. Morokuma, V.G. Zakrzewski, G.A. Voth, P. Salvador, J.J. Dannenberg, S. Dapprich, A.D. Daniels, O. Farkas, J.B. Foresman, J.V. Ortiz, J. Cioslowski, D.J. Fox, Gaussian Inc., Wallingford, Gaussian 09, Revision B.01., 2010.
[39] F.J. Devlin, P.J. Stephens, J.R. Cheeseman, M.J. Frisch, J. Phys. Chem. A 101 (1997) 9912-9924.
[40] S. Grimme, J. Antony, S. Ehrlich, H. Krieg, J. Chem. Phys. 132 (2010) 154104.
[41] A. Klamt, G. Schüürmann, J. Chem. Soc., Perkin Trans. 2 (1993) 799-805.
[42] S.P. de Visser, M.G. Quesne, B. Martin, P. Comba, U. Ryde, Chem. Commun. 50 (2014) 262-282.
[43] M.C. Durrant, Dalton Trans. 43 (2014) 9754-9765.
[44] P.A. Davethu, S.P. de Visser, J. Phys. Chem. A 123 (2019) 6527-6535.
[45] J.B. Kim, J.J. Leonard, F.R. Longo, J. Am. Chem. Soc. 94 (1972) 3986−3992.
[46] Q. Jia, N. Ramaswamy, H. Hafiz, U. Tylus, K. Strickland, G. Wu, B. Barbiellini, A. Bansil, E.F. Holby, P. Zelenay, S. Mukerjee, ACS Nano 9 (2015) 12496-12505.
[47] I. Hod, M.D. Sampson, P. Deria, C.P. Kubiak, O.K. Farha, J.T. Hupp, ACS Catal. 5 (2015) 6302-6309.
[48] W. Zhang, Y. Hu, L. Ma, G. Zhu, Y. Wang, X. Xue, R. Chen, S. Yang, Z. Jin, Adv. Sci. 5 (2018) 1700275.

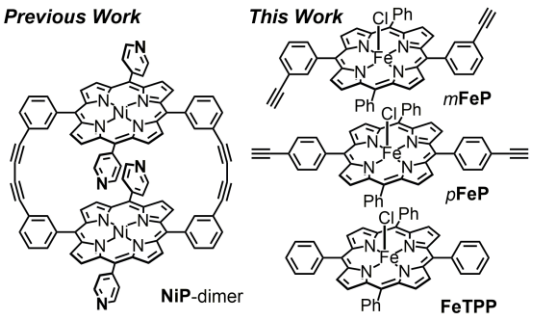

Figure 1. Molecular structures of **NiP**-dimer [27], ***m*FeP**, ***p*FeP**, and **FeTPP** reference.

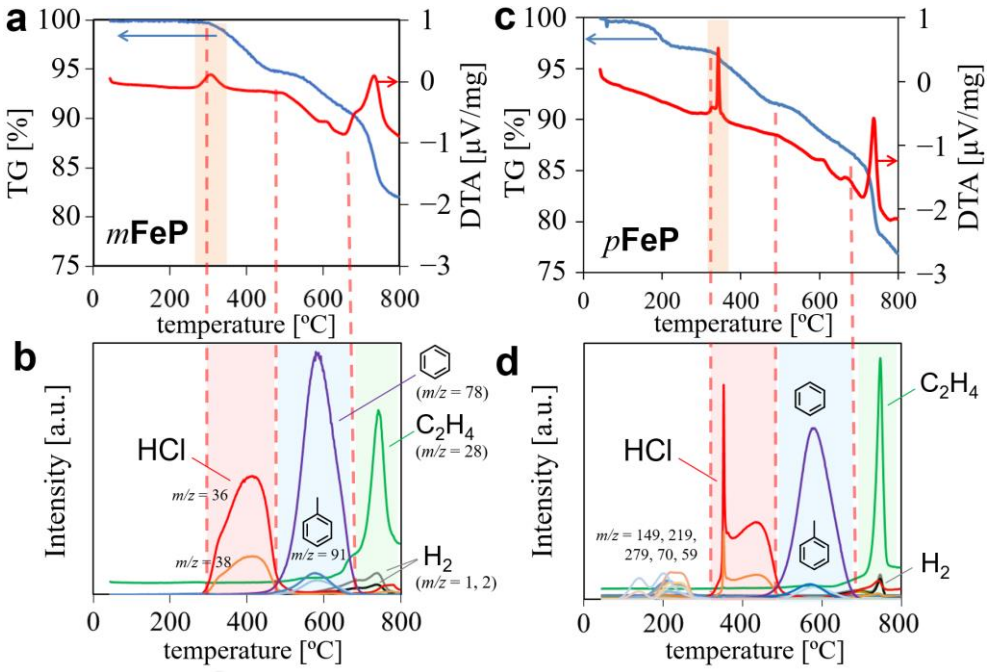

Figure 2. Simultaneous analysis of pyrolysis behavior of (a,b) ***m*FeP** and (c,d) ***p*FeP**: (a,c) TG-DTA and (b,d) time-course of mass spectrometry with the temperature elevated at 10 ºC min^{-1} under a steady flow of He (50 mL min^{-1}).

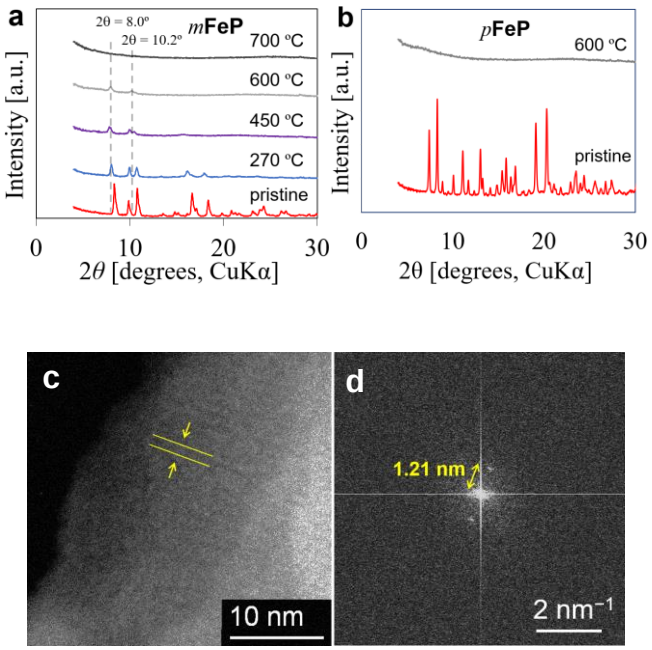

Figure 3. PXRD patterns of (a) ***m*FeP** and (b) ***p*FeP** annealed at the specified temperatures. (c) HAADF-STEM and (d) the SAED image of ***m*FeP** annealed at 600 ºC. The lattice spacing calculated from the reciprocal of the distance between the major SAED patterns is 1.21 nm.

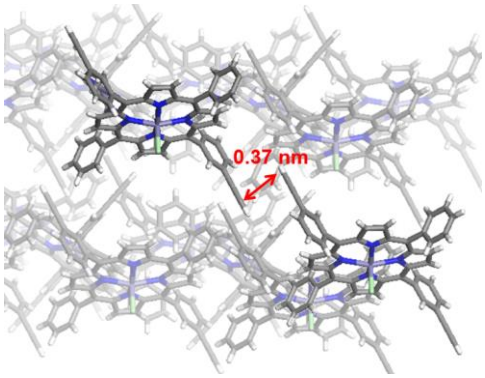

Figure 4. Crystal structure of original ***m*FeP** with chloride as an axial ligand. The structure was depicted after the modification of the disorder. The closest ethynyl groups were distanced by 0.37 nm. The detailed information is shown in Fig. S4.

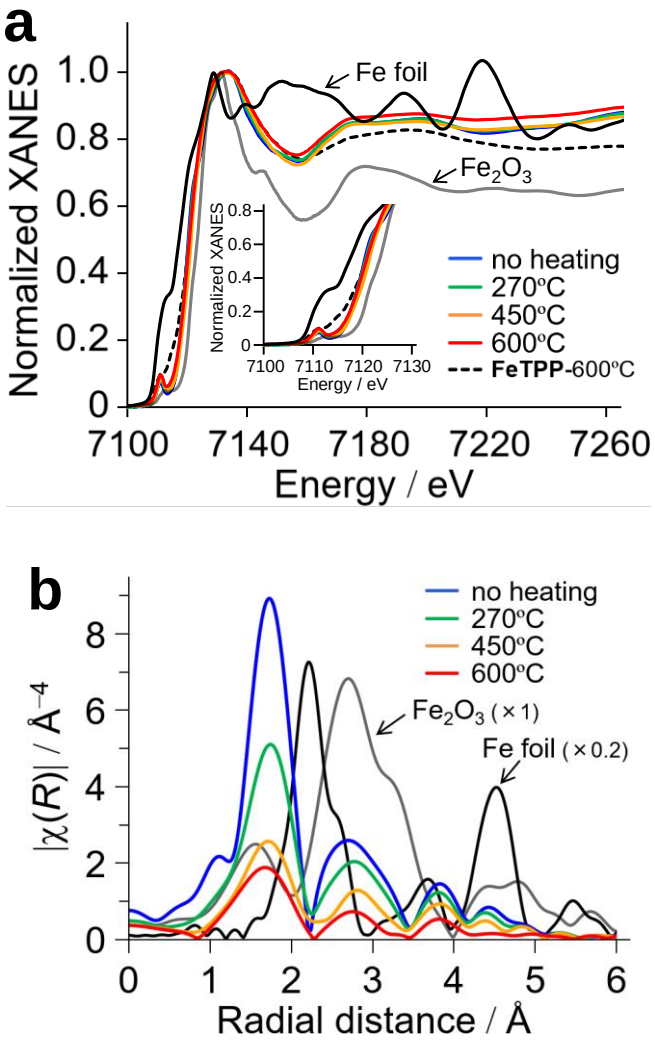

Figure 5. XAFS of *m***FeP** annealed at the specified temperature. (a) XANES and (b) pseudo-radial structural functions calculated from EXAFS patterns of the Fe K-edge (FT range, 2.0 to 10.5 $Å^{-1}$). The data of Fe foil and Fe_2O_3 are also shown for comparison.

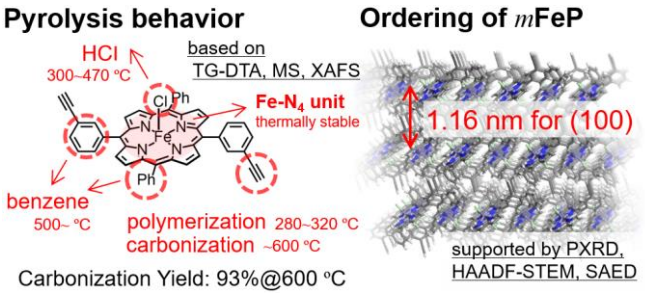

Figure 6. (left) Pyrolysis behavior of *m***FeP**: (1) thermal polymerization of ethynyl units (280~320 ºC); (2) removal of Cl atom (300~470 ºC); (3) partial removal of the phenyl groups (~500 ºC); (4) carbonization (~600 ºC); the tetrapyrrole-based π-conjugated structure was maintained with the planar Fe–N_4 unit. (right) The crystal structure of *m***FeP** showing the (100) spacing.

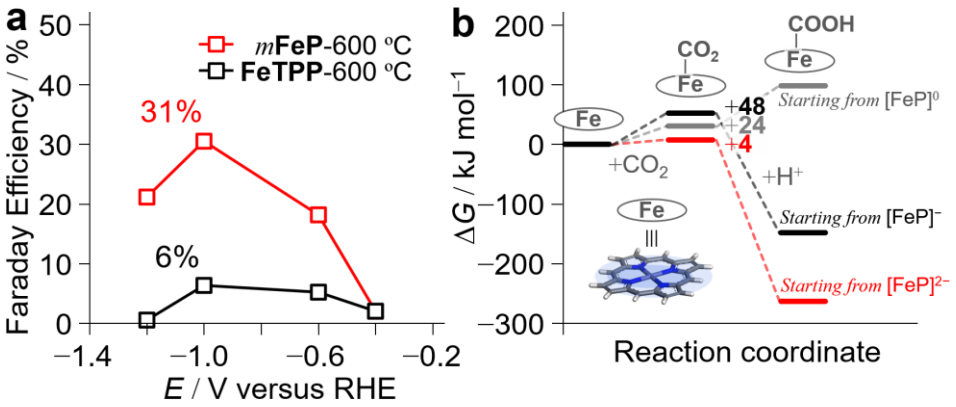

Figure 7. (a) Faraday efficiencies for electrochemical reduction of CO_2 using *m***FeP** (red) and **FeTPP** (black) annealed at 600 ºC at selected potentials versus the reversible hydrogen electrode (RHE). The remaining Faraday efficiency corresponds to H_2 evolution. (b) Energy level diagrams for the formation of CO_2 complexes and the subsequent proton-coupled electron transfer on single-site [FeP] starting from the specified oxidation states. Shown are results computed with conventional DFT at uB3LYP/6−311++G(d,p) level of theory. The details for electrochemistry and computational chemistry are summarized in Tables S2−S8.

Supporting Information for

Iron porphyrin-derived ordered carbonaceous frameworks

Masanori Yamamoto,[1,*] Kazuma Takahashi,[1] Mao Ohwada,[1] Yuxin Wu,[2] Kazuyuki Iwase,[1,3] Yuichiro Hayasaka,[4] Hisashi Konaka,[5] Henry Cove,[6] Devis Di Tommaso,[6] Kazuhide Kamiya,[2,3] Jun Maruyama,[7] Fumito Tani,[8] Hirotomo Nishihara[1,9,*]

[1] *Institute of Multidisciplinary Research for Advanced Materials, Tohoku University, 2−1−1 Katahira, Aoba-ku, Sendai, Miyagi, 980−8577, Japan*
[2] *Graduate School of Engineering Science, Osaka University, 1−3 Machikaneyama, Toyonaka, Osaka 560−8531, Japan*
[3] *Research Center for Solar Energy Chemistry, Osaka University, 1-3 Machikaneyama, Toyonaka, Osaka 560−8531, Japan*
[4] *The Electron Microscopy Centre, Tohoku University, 2−1−1 Katahira, Aoba, Sendai 980−8577, Japan*
[5] *Application & Software Development Department, X-ray Instrument Division, Rigaku Corporation, 3−9−12, Matsubara-cho, Akishima-shi, Tokyo 196−8666, Japan*
[6] *School of Biological and Chemical Sciences, Queen Mary University of London, Mile End Road, E1 4NS London, United Kingdom*
[7] *Research Division of Environmental Technology, Osaka Research Institute of Industrial Science and Technology, 1−6−50, Morinomiya, Jo-to-ku, Osaka 536−8553, Japan*
[8] *Institute for Materials Chemistry and Engineering, Kyushu University, Nishi-ku, Fukuoka 819−0395, Japan*
[9] *Advanced Institute for Materials Research (WPI-AIMR), Tohoku University, Katahira 2−1−1, Aoba-ku, Sendai, 980−8577, Japan*

*To whom correspondence should be addressed: masanori.yamamoto.b2@tohoku.ac.jp; hirotomo.nishihara.b1@tohoku.ac.jp;

1. HRMS analysis

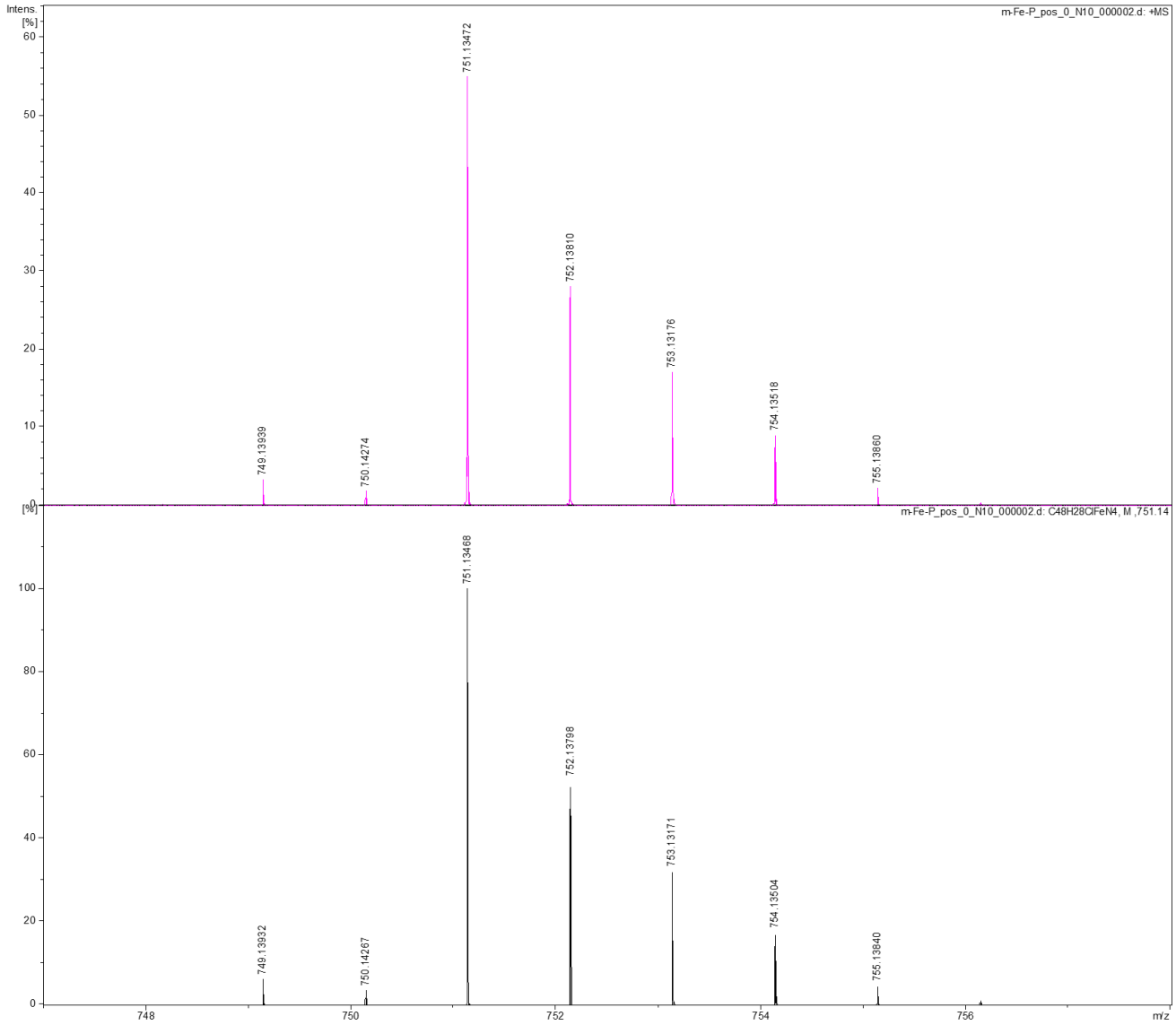

Figure S1. MALDI-TOF-HRMS of *m***FeP** (top) and the simulation pattern calculated for $[M]^+$ (bottom).

2. *Dissolution test*

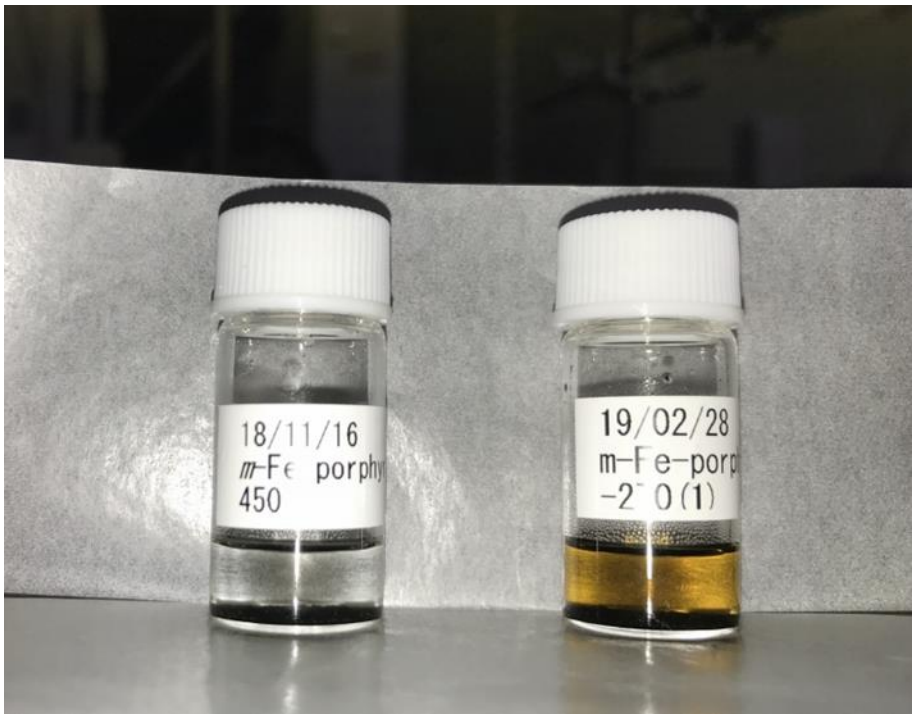

Figure S2. The photos of ***m*FeP** annealed at 270 ºC and 450 ºC (each ~5 mg) after the addition of CH_2Cl_2. For ***m*FeP** annealed at 270 ºC, very small amount of molecules was dissolved upon the addition of the solvent as confirmed by the color change, while no color change was observed for ***m*FeP** annealed at 450 ºC, indicating the efficient crosslinking upon the heating.

3. FE-SEM

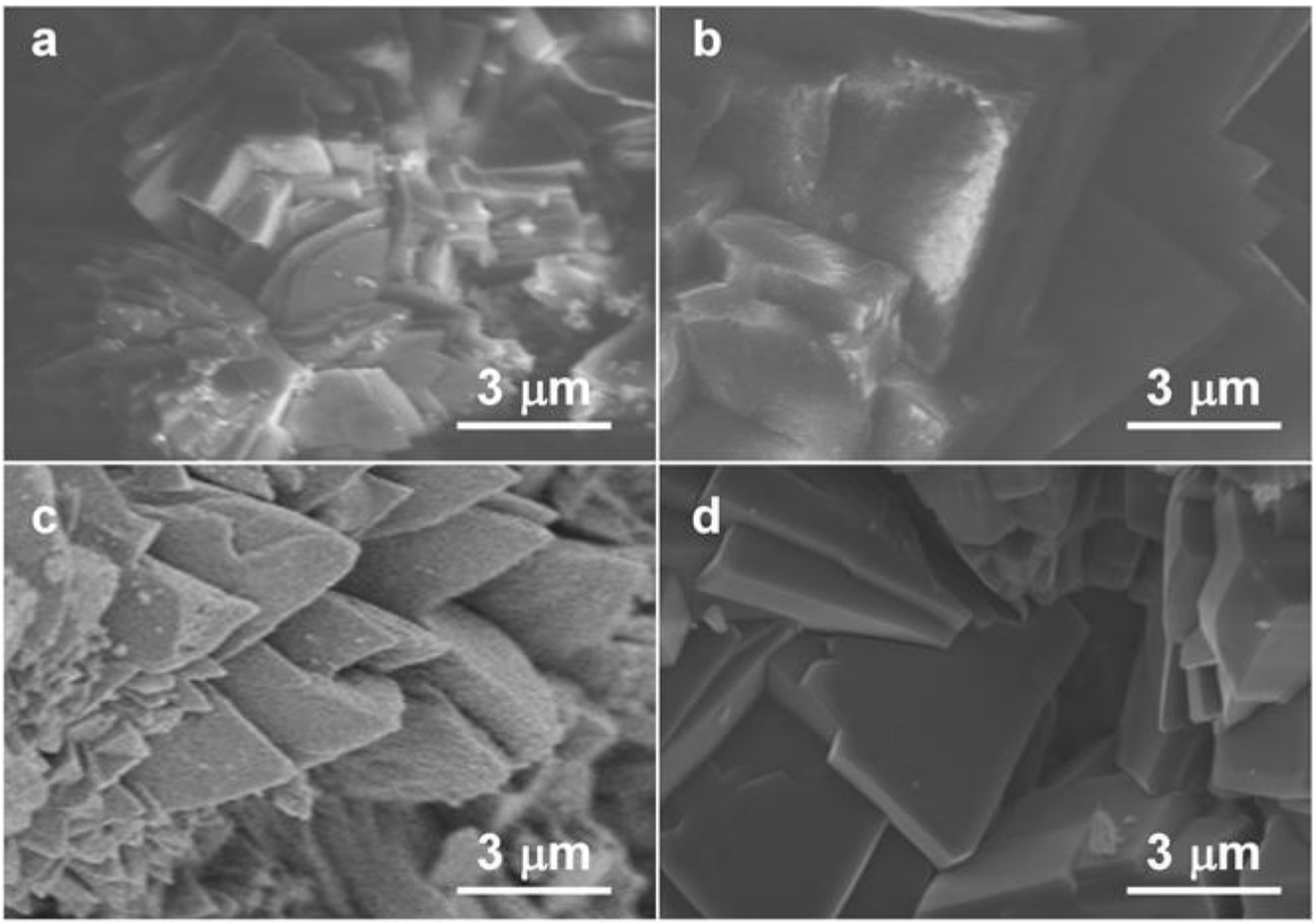

Figure S3. FE-SEM images of *m***FeP** as (a) the pristine crystal and as the treated samples annealed at (b) 270 ºC, (c), 450 ºC, and (c) 600 ºC. Since the sample annealed at 450 °C is easily decomposed by an electron beam, this sample was observed after Pt coating by sputtering.

4. PXRD crystallography

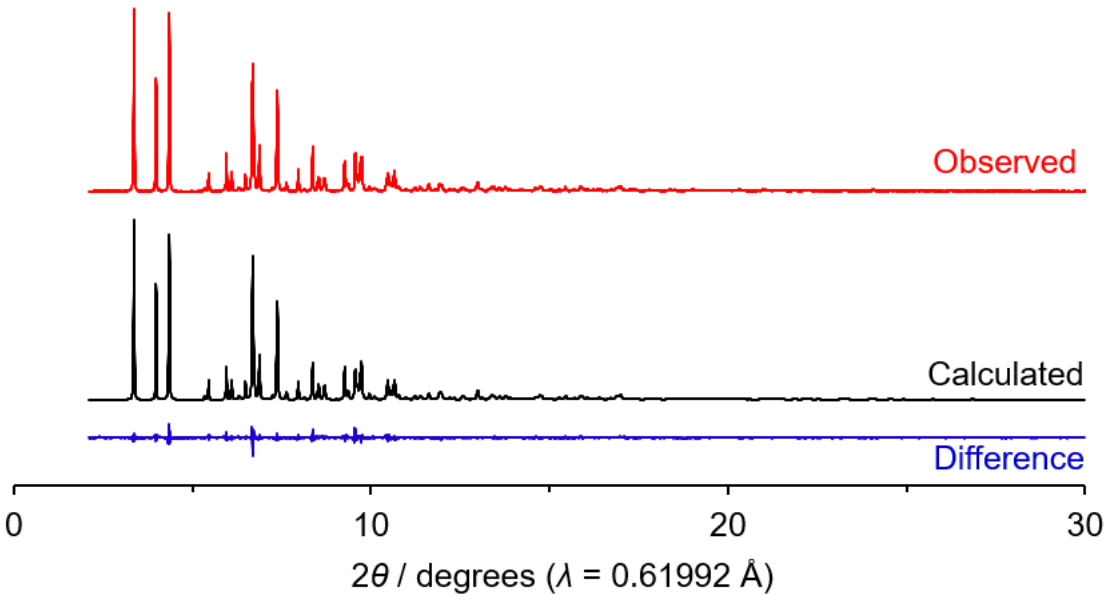

Figure S4. PXRD pattern and the profile fitting results of *m***FeP**. Crystallographic parameters, Formula: $C_{48}H_{28}N_4FeCl$, M: 752.061, Crystal system: monoclinic, Space group: $P12_1/c1$, a: 11.6001(9) Å, b: 13.3221(12) Å, c: 13.2191(9) Å, β: 114.4916(15)°, V: 1859.0(3) Å^3, Z: 2, T: 298 K, D_{calc}: 1.34 g cm^{-3}, R_{wp}: 5.28%, S: 1.61%. Crystallographic data (CIF file) have been deposited with the Cambridge Crystallographic Data Centre as supplementary publications (CCDC 1994452).

5. *ADF-STEM/EDS imaging*

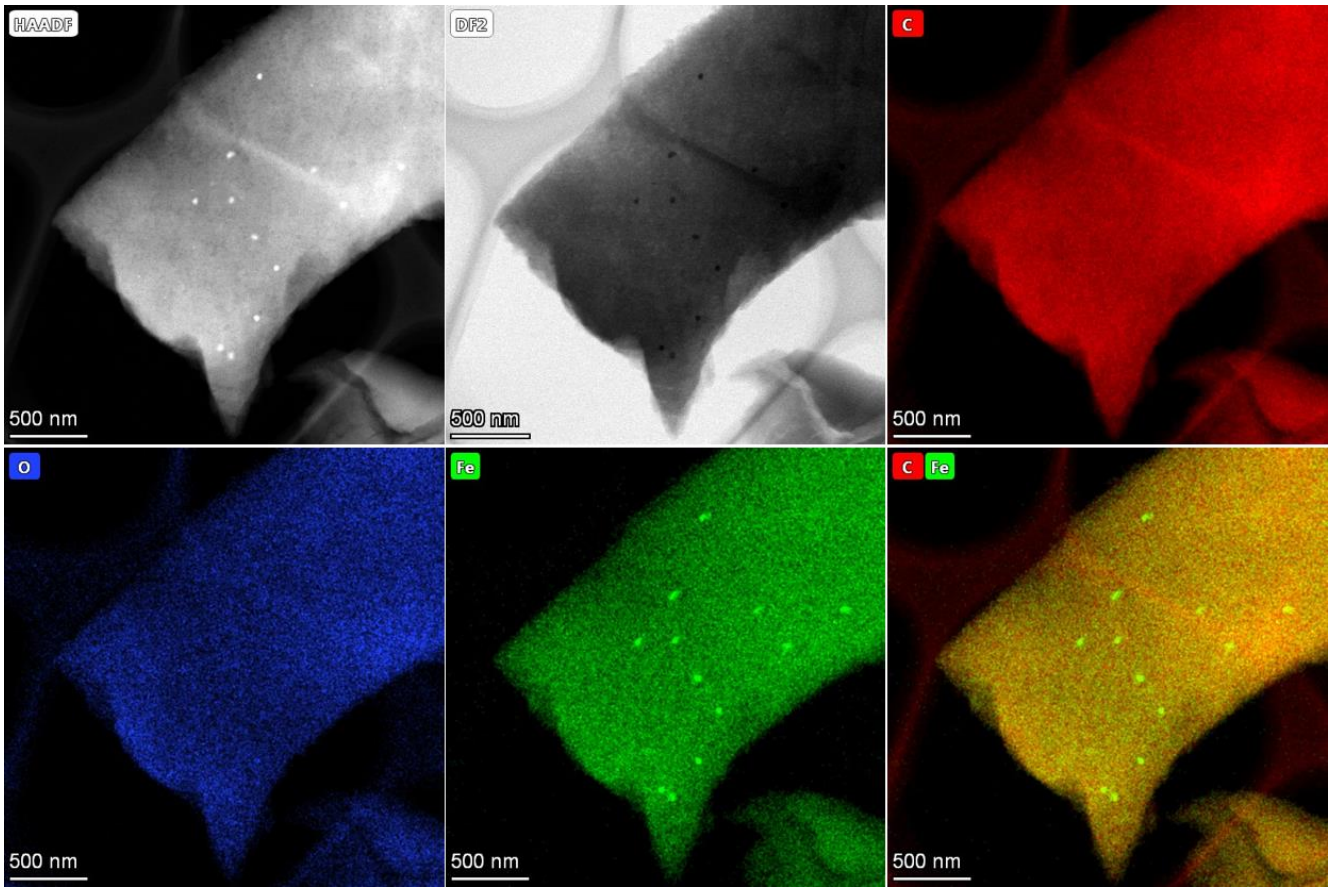

Figure S5. HAADF-STEM and EDS images of *m***FeP** annealed at 600 ºC.

6. *Porosity of the samples*

Table S1. Porosity of ***m*FeP** and ***p*FeP** after annealing.

Sample (annealing temperature)	BET surface area ($m^2\ g^{-1}$)	V_{N2} ($cm^3\ g^{-1}$)	V_{CO2} ($cm^3\ g^{-1}$)
***m*FeP** (450 °C)	0	0	0.13
***m*FeP** (600 °C)	5	0.001	0.17
***p*FeP** (600 °C)	22	0.023	n.m.[a]

[a] n.m.: Not measured.

7. *Cyclic voltammograms*

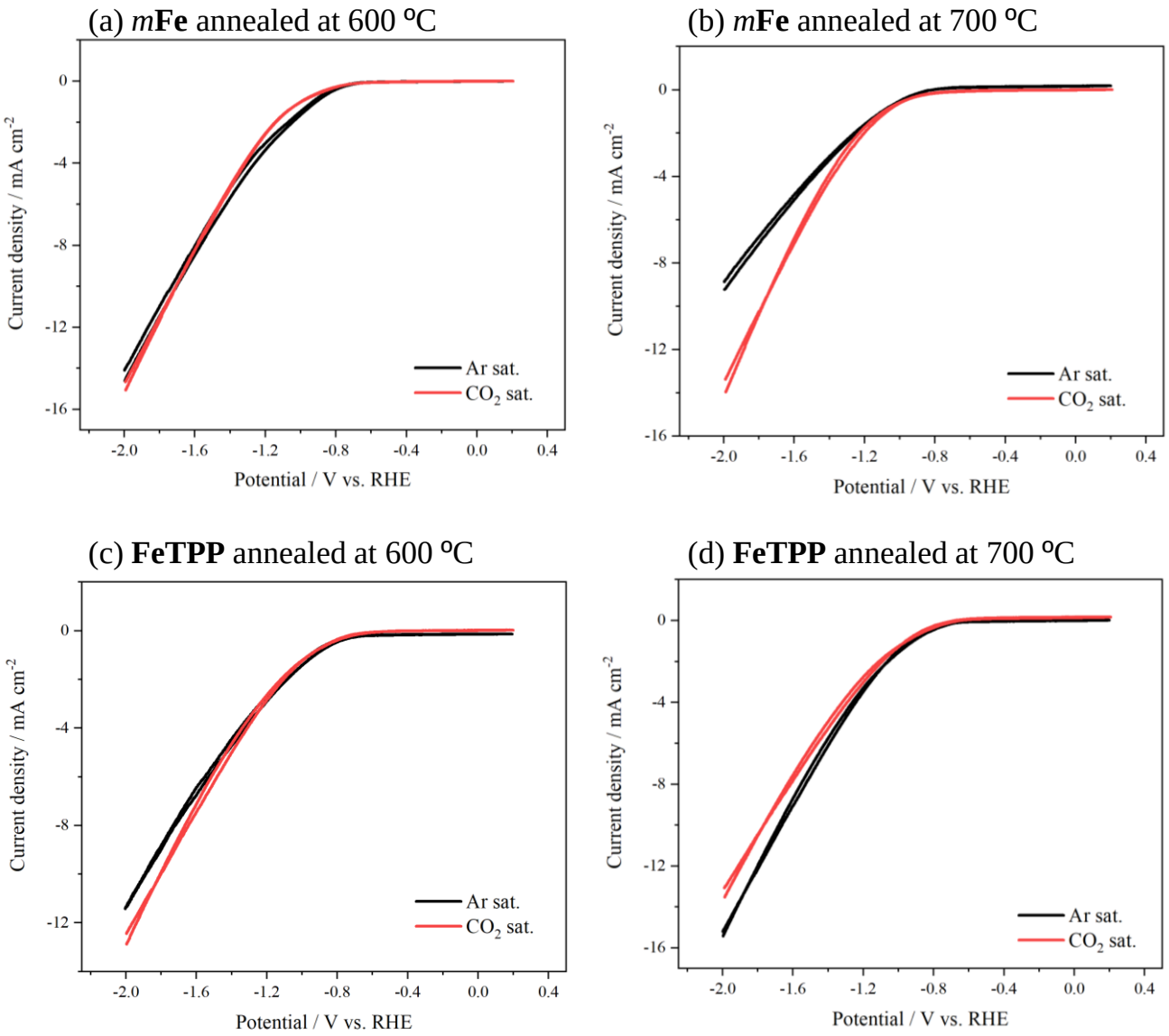

Figure S6. Cyclic voltammograms measured in 0.1 M phosphate buffer saturated with Ar and in 0.1 M $KHCO_3$ saturated with CO_2 (pH 6.8) for (a) ***m*FeP** annealed at 600 °C, (b) ***m*FeP** annealed at 700 °C, (c) **FeTPP** annealed at 600 °C, and (d) **FeTPP** annealed at 700 °C. Scan rate is 10 mV s^{-1}.

8. *Analysis of products during electrochemical CO_2 reduction*

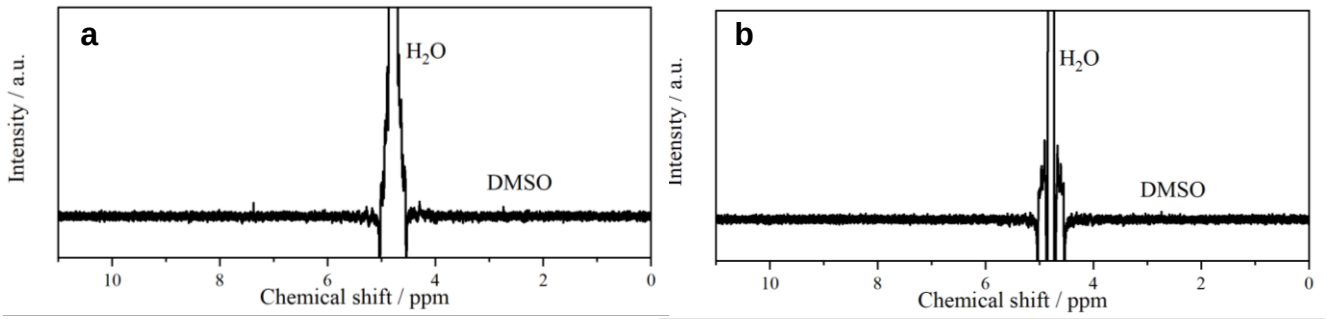

Figure S7. ^{1}H-NMR spectra of electrolytes after electrochemical reduction of CO_2 at -1.0 V vs RHE for 30 min using ***m*FeP** annealed at (a) 600 ºC and (b) 700 °C. DMSO was added as an internal standard.

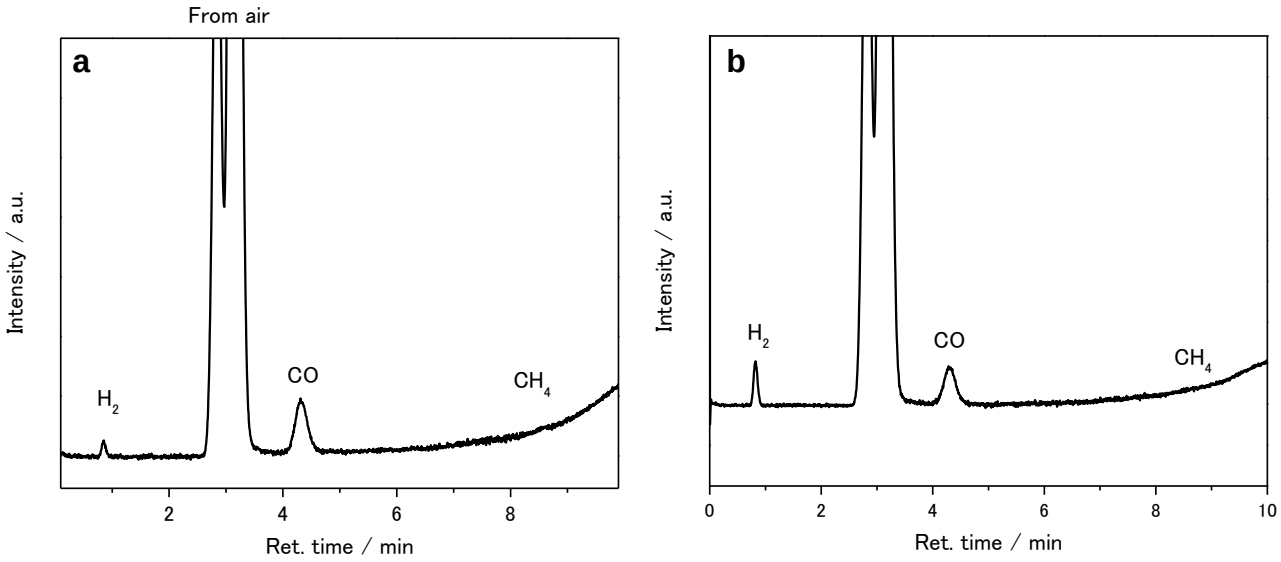

Figure S8. The results of GC-MS during electrochemical reduction of CO_2 (@1.0 V vs RHE, 30 min) using ***m*FeP** annealed at (a) 600 ºC and (b) 700 °C.

9. *Current efficiency data*

The results of electrochemical reduction of CO_2 were summarized in Tables S1−S4. The current density was reported in mA cm^{-2}. The total of Faraday efficiency is lower than 100% as often reported by other groups [1-4]. This is ascribed to the effect of oxygen-reduction reaction caused by a small amount of O_2 included as an impurity.

Table S2. Current efficiency data at different potentials using *m***FeP** calcined at 600 ºC.

Potential / V versus RHE	Faraday Efficiency			j_{sum}	j_{H2}	j_{CO}	j_{CH4}
	H_2	CO	CH_4				
−1.20	69.52	21.17	0.26	−3.99	−2.77	−0.84	−0.01
−1.00	35.15	30.51	0.48	−2.10	−0.74	−0.64	−0.01
−0.60	48.39	18.18	0.10	−1.61	−0.78	−0.29	−0.00
−0.40	30.72	2.05	0.14	−0.22	−0.07	−0.00	−0.00

Table S3. Current efficiency data at different potentials using *m***FeP** calcined at 700 ºC.

Potential / V versus RHE	Faraday Efficiency			j_{sum}	j_{H2}	j_{CO}	j_{CH4}
	H_2	CO	CH_4				
−1.20	83.52	0.40	0.18	−7.20	−6.01	−0.03	−0.01
−1.00	77.53	2.49	0.14	−2.87	−2.22	−0.07	−0.00
−0.60	63.47	16.63	0.31	−0.87	−0.55	−0.15	−0.00
−0.40	79.05	1.17	0.76	−0.42	−0.33	−0.00	−0.00

Table S4. Current efficiency data at different potentials using **FeTPP** calcined at 600 ºC.

Potential / V versus RHE	Faraday Efficiency			j_{sum}	j_{H2}	j_{CO}	j_{CH4}
	H_2	CO	CH_4				
−1.20	96.57	0.56	0.10	−5.04	−4.87	−0.03	−0.01
−1.00	77.74	6.36	0.49	−5.17	−4.02	−0.33	−0.03
−0.60	65.27	5.25	0.33	−1.01	−0.66	−0.05	−0.00
−0.40	82.34	2.08	0.96	−0.43	−0.35	−0.01	−0.00

Table S5. Current efficiency data at different potentials using **FeTPP** calcined at 700 ºC.

Potential / V versus RHE	Faraday Efficiency			j_{sum}	j_{H2}	j_{CO}	j_{CH4}
	H_2	CO	CH_4				
−1.20	92.02	1.03	0.28	−9.09	−8.36	−0.09	−0.03
−1.00	93.93	0.68	0.28	−4.95	−4.65	−0.03	−0.01
−0.60	66.53	3.09	0.32	−2.73	−1.82	−0.08	−0.01
−0.40	80.82	8.04	0.61	−1.10	−0.89	−0.09	−0.01

10. *Density functional theory calculations*

Density functional theory (DFT) calculations have been conducted to elucidate the mechanism of electrochemical reduction of CO_2 to CO on the iron porphine [FeP] complex. DFT calculations were conducted at the UB3LYP-D3 functional together with the double-ζ 6-31+G(d,p) (**BS1**) and the triple-ζ 6−311+G(d,p) (**BS2**) basis sets to treat all atoms. Solvation effects were treated using the continuum polarized conductor model (CPCM) to model the aqueous environment. For calculations at all levels, the minimum character of all optimized structures was verified by evaluation of the harmonic vibrational frequencies (no negative frequencies). Full details of the spin energetics are listed in **Table S6**.

In a previous DFT study, Davethu and Visser proposed a 2-electron catalytic cycle for the CO_2 reduction to CO by iron-porphyrins that involves a reduction, CO_2 binding, two protonations, and another reduction step [5]. In this reaction pathway, the CO_2 adsorption takes place with the iron center in the doubly reduced oxidation state, $[Fe]^{2-}$. In this study, we have characterized the structure and energetics of the intermediates along three alternative reaction mechanisms, depending on the initial oxidation state of the iron center: **pathway 1**, CO_2 adsorption on the $[FeP]^0$ complex; **pathway 2**, CO_2 adsorption on the $[FeP]^-$ complex; **pathway 3**, CO_2 adsorption on the $[FeP]^{2-}$ complex.

Table S7 reports the free energies of the elementary steps involved in reaction pathways 1-3: CO_2 adsorption onto the iron center (**step 1**); protonation of the $[Fe(CO_2)]$ intermediate (**step 2**); protonation of the [Fe(C(OH)O)] intermediate to form bound CO, [Fe(CO)] (**step 3**); electron transfer to the [Fe(CO)] intermediate to release CO (**step 4**); electron transfer to reduce [FeP] to its starting oxidation state (**step 5**). In steps 2 and 5, H_3O^+ was used as proton source. However, we have verified that the use of other common acid base pairs made negligible differences on the computed energetics of reaction. Since iron porphyrins can appear in a range of low-energy spin states, we computed the structures of [FeP] in all accessible spin states. We consider the doublet or quartet spin state for the $[Fe]^0$, $[Fe]^{2-}$, $[Fe(CO_2)]^0$, $[Fe(CO_2)]^{2-}$, $[Fe(C(OH)O)]^+$, $[Fe(C(OH)O)]^-$, $[Fe(CO)]^0$, and $[Fe(CO)]^{2+}$ complexes; the remaining complexes could adopt either a doublet or quartet spin state. The reaction energies reported in **Table S7** are between the lowest energy states. In the following discussion all values refer to the UB3LYP/BS2/CPCM level of theory.

For **step 1**, the adsorption of CO_2 onto the metal center appears marginally endergonic ($\Delta G > 0$) along all reaction pathways. Previous DFT calculations of CO_2 adsorption on copper nanoparticles have proposed as descriptor for the activation of CO_2 the bending of the molecule. The O=C=O angle of adsorbed CO_2 on the $[FeP]^0$ complex remains linear, whereas in the $[Fe(CO_2)]^-$ and $[Fe(CO_2)]^{2-}$complexes the CO_2 molecule adopts a bent structure. Therefore, from this result alone one would presume that reaction pathway 3 is the most energetically feasible. In **step 2**, the proton donor (H_3O^+) approaches the complex and delivers a proton to give $[Fe(C(OH)O)]^-$. This free energy of this step displays large differences amongst the three reaction pathways. The reaction free energies of pathway 2, $[Fe(CO_2)]^- + H_3O^+ \rightarrow [Fe(C(OH)O]^0 + H_2O$ (−46.19 kJ mol^{-1}), and pathway 3, $[Fe(CO_2)]^- + H_3O^+ \rightarrow [Fe(C(OH)O]^0 + H_2O$ (−46.19 kJ mol^{-1}) (−64.17 kJ mol^{-1}) are both feasible. On the other hand, the $[FeP(CO_2)]^0$ intermediate has a positive protonation free energy (12.15 kJ mol^{-1}). This may be explained by the reduced nucleophilicity of $[FeP(CO_2)]^0$ in comparison to $[Fe(CO_2)]^-$ and $[Fe(CO_2)]^{2-}$. The thermodynamic feasibility of step 2 along pathway 1 might be improved through the introduction of electron withdrawing substituents to the $[FeP(CO_2)]^0$ intermediate. **Step 3**, which involves the second protonation of the [FeP(C(OH)O)] intermediate, is significantly exergonic along all reaction

pathways. S**tep 4** corresponds to the desorption of a CO molecule. Energetics are largely negative for all three reaction pathways, especially for those associated with pathway 1, $[Fe(CO)]^{2+} + e^- \rightarrow CO + [Fe]^+$ (−120.51 kJ mol^{-1}), and pathway 2 $[Fe(CO)]^+ + e^- \rightarrow CO + [Fe]^0$ (−95.98 kJ mol^{-1}). The final step, **5**, involves a further reduction reaction to generate the iron porphine [FeP] complex in the initial oxidation state. Again, the regeneration of $[FeP]^0$ and $[FeP]^-$ along pathway 1 (−90.04 kJ mol^{-1}) and pathway 2 (−46.36 kJ mol^{-1}) are thermodynamically very favorable.

Table S6. Absolute (free) energies (in Hartees) calculated at the DFT(UB3LYP-D3) using the CPCM model to simulate water. BS1 = 6-31G+(d,p), BS2 = 6-311G++(d,p).

	E [BS1]	E+ZPE [BS1]	G [BS1]	ZPE [BS1]	E [BS2]	E + ZPE [BS2]	G [BS2]	ZPE [BS2]
[FeP]								
^{3}[Fe]	-2252.180746	-2251.906328	-2251.95188	0.274418	-2252.471741	-2252.198454	-2252.244052	0.273287
^{5}[Fe]	-2252.188798	-2251.917102	-2251.962298	0.271696	-2252.456554	-2252.184697	-2252.230233	0.271857
^{2}[Fe]$^+$	-2251.980687	-2251.709976	-2251.75596	0.270712	-2252.272458	-2252.000251	-2252.045228	0.272206
^{4}[Fe]$^+$	-2252.006026	-2251.732878	-2251.777014	0.273148	-2252.292061	-2252.017912	-2252.063562	0.274148
^{2}[Fe]$^-$	-2252.299125	-2252.026112	-2252.071042	0.273013	-2252.573655	-2252.301735	-2252.346655	0.27192
^{4}[Fe]$^-$	-2252.292209	-2252.021557	-2252.067746	0.270652	-2252.576306	-2252.309008	-2252.354934	0.267298
^{3}[Fe]$^{2-}$	-2252.377394	-2252.111818	-2252.157888	0.265577	-2252.655956	-2252.387729	-2252.43309	0.268227
^{5}[Fe]$^{2-}$	-2252.364016	-2252.097427	-2252.141831	0.26659	-2252.659884	-2252.393552	-2252.440748	0.266333
^{3}[Fe(HCO$_3$)]$^-$					-2517.136240	-2516.835592	-2516.888500	0.300648
^{2}[Fe(HCO$_3$)]$^{2-}$					-2517.239199	-2516.939765	-2516.993648	0.299434
^{3}[Fe(HCO$_3$)]$^{3-}$					-2517.338112	-2517.045386	-2517.100628	0.292726
^{3}[Fe(CO$_2$)]	-2440.799387	-2440.512294	-2440.564829	0.287093	-2441.128356	-2440.842231	-2440.894683	0.286125
^{5}[Fe(CO$_2$)]	-2440.789284	-2440.504466	-2440.560472	0.284818	-2441.112318	-2440.828264	-2440.883405	0.284055
^{2}[Fe(CO$_2$)]$^-$	-2440.906997	-2440.62155	-2440.66941	0.285448	-2441.231596	-2440.947045	-2440.996277	0.284551
^{4}[Fe(CO$_2$)]$^-$	-2440.900102	-2440.617074	-2440.667108	0.283028	-2441.225761	-2440.943723	-2440.994984	0.282038
^{3}[Fe(CO$_2$)]$^{2-}$	-2441.002853	-2440.721476	-2440.770308	0.281378	-2441.328999	-2441.048398	-2441.098888	0.280601
^{5}[Fe(CO$_2$)]$^{2-}$	-2440.997313	-2440.718235	-2440.769749	0.279079	-2441.325207	-2441.047076	-2441.098974	0.27813
^{3}[Fe(COOH)]$^+$	-2441.164743	-2440.86892	-2440.918941	0.295823	-2441.485387	-2441.188906	-2441.239174	0.296481
^{5}[Fe(COOH)]$^+$	-2441.151732	-2440.855609	-2440.90803	0.296123	-2441.465006	-2441.170076	-2441.222876	0.294931
^{2}[Fe(COOH)]	-2441.36605	-2441.066985	-2441.116503	0.299064	-2441.688389	-2441.390479	-2441.439958	0.29791
^{4}[Fe(COOH)]	-2441.343636	-2441.046834	-2441.09769	0.296802	-2441.666885	-2441.371248	-2441.422226	0.295637
^{3}[Fe(COOH)]$^-$	-2441.470926	-2441.175884	-2441.22611	0.295042	-2441.796828	-2441.502745	-2441.552988	0.294083
^{5}[Fe(COOH)]$^-$	-2441.488713	-2441.19533	-2441.245917	0.293383	-2441.815254	-2441.52279	-2441.57483	0.292464
^{3}[Fe(CO)]	-2365.521928	-2365.241111	-2365.29278	0.280816	-2365.82563	-2365.545933	-2365.597977	0.279697
^{5}[Fe(CO)]	-2365.516217	-2365.236876	-2365.288099	0.27934	-2365.82016	-2365.541979	-2365.593466	0.278181
^{2}[Fe(CO)]$^+$	-2365.334204	-2365.050514	-2365.099368	0.28369	-2365.634813	-2365.352329	-2365.402619	0.282485
^{4}[Fe(CO)]$^+$	-2365.346013	-2365.06389	-2365.114933	0.282122	-2365.647734	-2365.366771	-2365.41802	0.280964
^{3}[Fe(CO)]$^{2+}$	-2365.114495	-2364.833018	-2364.882201	0.281477	-2365.413289	-2365.132926	-2365.18205	0.280363
^{5}[Fe(CO)]$^{2+}$	-2365.128512	-2364.846741	-2364.897295	0.281771	-2365.428402	-2365.147848	-2365.198443	0.280555
Small molecules								
CO_2	-188.5934985	-188.582036	-188.602753	0.011462	-188.6499723	-188.638405	-188.659756	0.011567
CO	-113.3181246	-113.313121	-113.332258	0.005003	-113.3498347	-113.344809	-113.36393	0.005025
H_2O	-76.44236072	-76.421164	-76.43882	0.021197	-76.46654828	-76.445346	-76.46365	0.021202
H_3O^+	-76.82790838	-76.794902	-76.812299	0.033007	-76.85135306	-76.818245	-76.837329	0.033108

Table S7. Relative free energies for individual reactions in the reaction cycle as calculated at the DFT (UB3LYP-D3) level using the CPCM implicit solvation model (water). Values in kJ mol^{-1}.

	Reaction	ΔG for each step	
		6-31G+(d,p)	6-311G++(d,p)
	Pathway 1		
Step 1	$[Fe]^0 + CO_2 \rightarrow [Fe(CO_2)]^0$	+0.14	+5.73
Step 2	$[Fe(CO_2)]^0 + H_3O^+ \rightarrow [Fe(C(OH)O]^+ + H_2O$	+12.15	+18.32
Step 3	$[Fe(C(OH)O)]^+ + H_3O^+ \rightarrow [Fe(CO)]^{2+} + 2H_2O$	−27.42	−30.90
Step 4	$[Fe(CO)]^{2+} + e^- \rightarrow CO + [Fe]^+$	−109.80	−120.51
Step 5	$[Fe]^+ + e^- \rightarrow [Fe]^0$	−93.05	−90.04
	Pathway 2		
Step 1	$[Fe]^- + CO_2 \rightarrow [Fe(CO_2)]^-$	+2.75	+11.55
Step 2	$[Fe(CO_2)]^- + H_3O^+ \rightarrow [Fe(C(OH)O]^0 + H_2O$	−46.19	−43.93
Step 3	$[Fe(C(OH)O)]^0 + H_3O^+ \rightarrow [Fe(CO)]^+ + 2H_2O$	−40.02	−42.69
Step 4	$[Fe(CO)]^+ + e^- \rightarrow CO + [Fe]^0$	−89.50	−95.98
Step 5	$[Fe]^0 + e^- \rightarrow [Fe]^-$	−45.02	−46.36
	Pathway 3		
Step 1	$[Fe]^{2-} + CO_2 \rightarrow [Fe(CO_2)]^{2-}$	−6.07	+1.01
Step 2	$[Fe(CO_2)]^{2-} + H_3O^+ \rightarrow [Fe(C(OH)O]^- + H_2O$	−64.09	−64.17
Step 3	$[Fe(C(OH)O)]^- + H_3O^+ \rightarrow [Fe(CO)]^0 + 2H_2O$	−70.41	−70.98
Step 4	$[Fe(CO)]^0 + e^- \rightarrow CO + [Fe]^-$	−46.13	−52.64
Step 5	$[Fe]^- + e^- \rightarrow [Fe]^{2-}$	−31.28	−30.63

Table S8. Comparison of the energetics of adsorption of the bicarbonate (HCO_3^-) and carbon dioxide (CO_2) molecules on the iron complexes $[FeP]^0$, $[FeP]^-$ and $[FeP]^{2-}$ as calculated at the DFT (UB3LYP-D3/6-311G++(d,p)) level using the CPCM implicit solvation model (water). Values in kJ mol^{-1}.

	ΔE	**ΔE + ZPE**	**ΔG**
Pathway 1			
$[Fe]^0 + HCO_3^- + H_2O \rightarrow [Fe(CO_3H)]^-$	-5.65	-4.73	6.85
$[Fe]^0 + CO_2 \rightarrow [Fe(CO_2)]^0$	-4.17	-3.37	5.73
Pathway 2			
$[Fe]^- + HCO_3^- \rightarrow [Fe(CO_3H)]^{2-}$	-4.63	-0.73	10.42
$[Fe]^- + CO_2 + \rightarrow [Fe(CO_2)]^-$	-3.34	0.23	11.55
Pathway 3			
$[Fe]^{2-} + HCO_3^- \rightarrow [Fe(CO_3H)]^{3-}$	-14.27	-13.95	0.32
$[Fe]^{2-} + CO_2 \rightarrow [Fe(CO_2)]^{2-}$	-12.01	-10.32	1.01

11. Reference

[1] J. Choi, P. Wagner, R. Jalili, J. Kim, D.R. MacFarlane, G.G. Wallace, D.L. Officer, Adv. Energy Mater. 8 (2018) 1801280.

[2] P. De Luna, R. Quintero-Bermudez, C.-T. Dinh, M.B. Ross, O.S. Bushuyev, P. Todorović, T. Regier, S.O. Kelley, P. Yang, E.H. Sargent, Nat. Catal. 1 (2018) 103-110.

[3] W. Ju, A. Bagger, G.-P. Hao, A.S. Varela, I. Sinev, V. Bon, B. Roldan Cuenya, S. Kaskel, J. Rossmeisl, P. Strasser, Nat. Commun. 8 (2017) 944.

[4] S. Rasul, D.H. Anjum, A. Jedidi, Y. Minenkov, L. Cavallo, K. Takanabe, Angew. Chem. Int. Ed. 54 (2015) 2146-2150.

[5] P.A. Davethu, S.P. de Visser, J. Phys. Chem. A 123 (2019) 6527-6535.

Credit Author Statement

Masanori Yamamoto: Design of experiments and methodology, Writing original draft
Kazuma Takahashi: Material synthesis and major characterization
Mao Ohwada: Data curation for pyrolysis behavior
Yuxin Wu: Data curation for electrochemistry
Kazuyuki Iwase: Data curation for electrochemistry
Yuichiro Hayasaka: Data curation for STEM HAADF and EDX
Hisashi Konaka: Support for powder X-ray crystallography
Henry Cove: Theoretical calculations
Devis Di Tommaso: Theoretical calculations
Kazuhide Kamiya: Design of electrochemical measurement
Jun Maruyama: XAFS analysis
Fumito Tani: Design of molecules and experiments
Hirotomo Nishihara: Conceptualization, Reviewing and editing

*Declaration of Interest Statement

Declaration of interests

☐ The authors declare that they have no known competing financial interests or personal relationships that could have appeared to influence the work reported in this paper.

☒The authors declare the following financial interests/personal relationships which may be considered as potential competing interests:

This work was supported by JST CREST Grant Number JPMJCR18R3; JSPS KAKENHI Grant Number 19K15281; and the Cooperative Research Program for CORE lab of “Five-star Alliance” in “NJRC Mater. & Dev.”